Supplementary Information (SI) for Inorganic Chemistry Frontiers.

[2+2] photocycloaddition induces 114 K high-temperature shift of spin crossover transition - the role of the cycloaddition induced strain

Marcin Kaźmierczak,[a*] Vladyslav Maliuzhenko,[a] Aleksandra Tołoczko,[a] Marek Weselski,[a] Miłosz Siczek,[a] Juliusz A. Wolny,[b] Volker Schünemann[b] and Robert Bronisz[a*]

[a] *Faculty of Chemistry, University of Wrocław, F. Joliot-Curie 14, 50-383, Wrocław, Poland.*

[b] *Faculty of Physics, RPTU Kaiserslautern-Landau, Erwin Schrödinger Str. 46 67663 Kaiserlautern, Germany*

Contents: page

Materials and methods 2
Scheme S1. Synthesis of 6-(1,2,3-triazol-1-ylmethyl)coumarin (**L1**) 4
Synthesis of 6-methylcoumarin, 6-bromomethylcoumarin, 6-(1,2,3-triazol-1-ylmethyl)coumarin (**L1**), [Fe(L1)$_6$](BF$_4$)$_2$·2CH$_3$CN (**1**), [Fe(L1)$_6$](BF$_4$)$_2$ (**2**) 4-6
Photoconversion 1 → 1c and **2 → 2c** 6
^{1}H NMR spectra of 1c and 2c 7
Table S1. Crystallographic data for crystal structures of **1** and **1c** 8
Table S2. Crystallographic data for crystal structures of **2** and **2c** 9-10
Table S3. Values of torsion angles involving the methylene group in **2** and **2c** 10
Table S4. Values of torsion angles N-Fe-N—C(triazole) for **1**, **1c**, **2** and **2c**. 11
Figure S1. The coordination environment of Fe(II) in **1** 12
Figure S2. Overlapping of coumarin fragments in **1** 12
Figure S3. Mössbauer spectra for **1** and **1c** 13
Figure S4. Temperature dependences of χ_MT, relative areas of HS form derived from Mossbauer spectroscopy and relative shortening of Fe-N distances (SC-XRD) for **1** and **1c** 14
Figure S5. The coordination environment of Fe(II) and structure of dimerized ligands in **1c** 15
Figure S6. FTIR spectra of **1** (a) and **1c** (b) in nujol mulls 16
Comment to LIESST and r-LIESST experiments in **1** and **1c** 17
Figure S7. χ_MT(T) dependences recorded for LIESST and LITH experiments for **1** and **1c** 17
Comment to LIESST and r-LIESST experiments in **2** 18
Figure S8. χ_MT(T) dependences recorded for LIESST, LITH and r-LIESST experiments for **2** 18-19
Figure S9. The coordination environment of Fe(II) for **2** and **2c** 20
Figure S10. Mössbauer spectra for **2** at 200 K and 48 K 21
Figure S11. FTIR spectra of **2** (a) and **2c** (b) in nujol mulls 22
Comment on the analysis of structural changes induced by the [2+2] photocycloaddition 23
Figure S12. Structure of the ligand in its dimeric form in complexes obtained through the [2+2] cycloaddition reaction for compounds: **2c** and tetrazole analogue 23-24
Figure S13. Mössbauer spectra showing photoconversion **2** → **2c** 25
Comment to LIESST and r-LIESST experiments **2c** 26
Figure S14. χ_MT(T) dependences recorded for LIESST and LITH experiments for **2c** 26
Figure S15. PXRD diffractograms for **1** and **1c** 27
Figure S16. PXRD diffractograms for **2** and **2c** 28
Comment concerning intermolecular contacts in 1 and 1c 29
Comment concerning intermolecular contacts in 2 and 2c 29
DFT modelling 30
Figure S17 The structural model used for the DFT modelling of **2c** 30
Figure S18 The structural model used for the DFT modelling of **2** 31
Tables S5a-f. Electronic energy differences ΔE (kJ·mol^{-1}) of photodimerised ligands corresponding to the whole molecules (a), cyclobutane together with coumarin fragments (b), phenyl fragments (c), cyclobutane together with lactone fragments (d), triazole rings (e) and isolated cyclobutane fragments in the HS and LS states of **2c**. 32-34
References 35

Materials and methods

Acetonitrile (HPLC grade, J.T. Baker) was dried by distillation over the calcium hydride. *N*-bromosuccinimide (Merck), 1*H*-1,2,3-triazole (Chemical Point), iron(II) perchlorate hexahydrate (Alfa Aesar; reagent grade) were used as delivered. Benzoyl peroxide (Merck) was recrystallized from anhydrous methanol (distilled over magnesium methoxide).

Syntheses of iron(II) complexes were carried out under a nitrogen atmosphere using the standard Schlenk technique.

Elemental analyses for carbon, hydrogen and nitrogen were carried out using Vario ELcube analyzer. FTIR microscopy spectra in the range 4000-900 cm^{-1} (CaF_2 window) region were measured with a JASCO FT/IR-6700 infrared microscope. ^{1}H and ^{13}C NMR spectra were recorded on Bruker Avance III 500 MHz spectrometer at room temperature. Temperature dependent measurements of the magnetic susceptibility for **1** and **2** were carried out with a Quantum Design MPMS3 magnetometer under 1 T applied magnetic field. Measurements for **1** and **1c** were carried out for samples wetted with acetonitrile and placed in sealed glass tube. Measurements for **2** and **2c** were carried out in polyethylene holder. Light induced spin state switching experiments (SQUID) were carried out using laser lights of wavelength 532 nm or 808 nm. Light power was adjusted to 5 and 3 mW, respectively, which allowed to maintain stable temperature. The weight of the samples were found by comparison with magnetic susceptibility of accurately weighted sample. Data have been corrected for the signal of the empty holder and for diamagnetism of the samples. Mössbauer spectra were recorded using ^{57}Co/Rh source (*ca.* 10 mCi) on POLON spectrometer working at constant acceleration mode. Lakeshore 200 device was used for temperature control. The samples of **1** (moistened with acetonitrile) and **2**, which was enriched with ^{57}Fe up to *ca.* 8%, was placed in the sealed polyethylene container of diameter 16 mm and mounted on a cold finger of helium cryostat (ARS DMX-20 cooling system). LIESST experiment (Mössbauer cryostat) was carried out using laser light (200 mW) of wavelength 532 nm under continuous irradiation. Deconvolution of Mössbauer spectra was carried out by least-square fitting using Lorentzian functions (MOS software). The isomer shift δ and quadrupole splitting ΔE_Q were calculated in relation to α-Fe (295 K). Photoinduced [2+2] cyclisation was performed using a 1 W diode light source with a wavelength of 365 nm on samples that had been wetted with acetonitrile and sealed in a polyethylene container. Crystals of **1** and **2** intended for FTIR microscopy and SC-XRD studies were irradiated from a distance of 3 mm.

Single crystal X-ray data collection and structure determination.

The crystals of complexes **1** and **2** suitable for single crystal X-ray diffraction studies were obtained directly from syntheses of macroscopic samples. Single crystals of **1c** and **2c** were obtained by irradiation (365 nm, 1 W) of preselected single crystals of **1** and **2**, respectively. In order to dissociate compound **2c** a single crystal was placed on the Boetius stage at 180°C and the temperature was raised to 225-230°C (10°C/min). The crystal was held at this temperature for 5 minutes and then removed from the stage because starts its decomposition. Crystals were covered with oil and placed on a loop (MiTeGen) or a glass capillary. Structural studies were performed with a κ-geometry, four-circle XtaLAB Synergy-R DW (Rigaku) diffractometer with rotating anode using Mo-Kα (λ = 0.71073 Å) radiation and Hybrid Pixel Array Detector 150° (Rigaku) or with Kuma a KM4-CCD κ-geometry automated four-circle diffractometer equipped with a CCD camera Sapphire2 and graphite-monochromatized Mo Kα radiation (λ = 0.71073 Å). During low-temperature measurements, an Oxford Cryosystem cooling device was used. Low temperatures were achieved with a stream of cold nitrogen gas; the temperature stability was 0.1 K. CrysAlis^{Pro} software was used to control the measurement procedure, data reduction, determine and refine the lattice parameters. The crystal structures were solved by dual-space recycling with the SHELXT-2018 program.[1] The refinements were carried out with the SHELXL-2018/3 program[2] using the full-matrix least-squares method. Additionally OLEX2 was used as a refinement and analysis program.[3] Non-hydrogen atoms were refined with anisotropic thermal parameters and Hydrogen atoms were included from geometric considerations. In the final refinement stages a riding model was used for C–H bonds. During the refinement of the disordered fragments constraints on atomic displacement parameters (EADP instruction) and geometric restraints (SADI, SAME, RIGU instructions) were used if appropriate. CCDC 2490226-2490234 contain the supplementary crystallographic data for this paper. These data can be obtained free of charge from The Cambridge Crystallographic Data Centre via www.ccdc.cam.ac.uk/data_request/cif.

Computational methods.

The DFT calculation were performed with Gaussian 16[4] As described in the main text the TPSS exchange-correlation functional was used with the TZVP basis set and Grimme's D3 dispersion corrections. In order to estimate the difference between the strain of the photodimerized ligands in **2c** the calculations of single-point energy for all crystallographically independent ligands were performed for each geometry to yield the mean change of the electronic energies on going from LS to HS geometry of the complex. In further step the obtained values of the strain energy difference were decomposed into increments of particular parts of the molecule. Namely, as shown in Fig. 9 (main text) the energy difference for ligands without azole rings were performed followed by the further reduction of the molecule with the final stage being the cyclobutane rings.

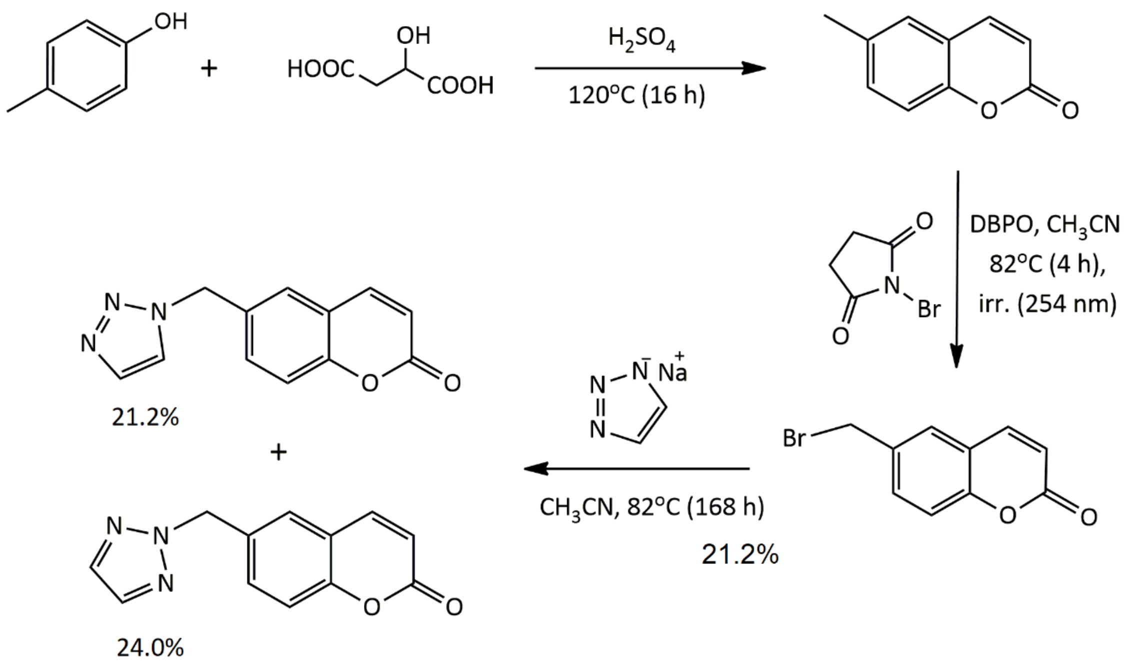

Scheme S1. Synthesis of 6-(1,2,3-triazol-1-ylmethyl)coumarin (**L1**).

Synthesis of 6-methylcoumarin

The synthesis was carried out following a literature procedure.[5] A mixture of 20.55 g of *p*-cresol (0.190 mol) and 25.47 g of malic acid (0.190 mol) was prepared. While maintaining the temperature at 0 °C, 50 ml of concentrated sulfuric acid was added dropwise. The resulting foaming mixture was then gradually heated and reached a temperature of 120°C within 4 hours. It was kept at this temperature for an additional 16 hours. The dark oil obtained was washed with ice-cold distilled water (2 × 30 ml), then extracted with 10 portions of hexane (80 ml each) at 60 °C. The combined organic fractions were concentrated under reduced pressure to give 3.18 g of a white solid product (yield: 10.4%).

Elemental analysis, found: C, 74.8%; H, 5.2%.

Calculated for $C_{10}H_8O_2$ (M = 160.17 g mol^{-1}): C, 75.0%; H, 5.0%.

^1H NMR (500 MHz, CD_3CN) δ [ppm]: 2.38 (s, 3H), 6.35 (d, 1H, J = 9.6 Hz), 7.22 (m, 1H), 7.39 (m, 2H), 7.79 (d, 1H, J = 9.6 Hz).

Synthesis of 6-bromomethylcoumarin

The synthesis was carried out according to a modified procedure reported in the literature.[6] To a round-bottomed quartz flask containing 80 mL of acetonitrile, 6-methylcoumarin (3.18 g, 19.9 mmol), *N*-bromosuccinimide (4.25 g, 24.0 mmol), and benzoyl peroxide (0.0248 g, 0.102 mmol) were added. The mixture was refluxed for 4 hours while simultaneously irradiating the flask contents with a mercury lamp. After this period, the reaction mixture was cooled to room temperature, and the solvent was removed under reduced pressure. The residue was treated with 150 ml of 1% aqueous potassium hydroxide and extracted with ethyl acetate (4 × 80 ml). The combined organic layers were washed with brine, dried over sodium sulfate (Na_2SO_4), and the solvent was evaporated under reduced pressure.

The crude product was recrystallized from acetonitrile (18 ml), yielding 1.97 g of product (yield: 41.4%) as light-orange crystals.

Elemental analysis, found: C, 50.1%; H, 3.3%.

Calculated for $C_{10}H_7O_2Br$ (M = 239.07 g/mol): C, 50.2%; H, 3.0%.

^1H NMR (500 MHz, CD_3CN) δ [ppm]: 4.64 (s, 2H), 6.41 (d, 1H, J = 9.6 Hz), 7.31 (d, 1H, 8.5 Hz), 7.64 (m, 2H), 7.83 (d, 1H, J = 9.6 Hz).

Synthesis of 6-(1,2,3-triazol-1-ylmethyl)coumarin (L1)

A solution of NaOH (0.540 g, 13.5 mmol) in 6 ml of water was prepared, followed by the addition of 1,2,3-triazole (0.942 g, 13.5 mmol) dissolved in 12 ml of water. The resulting clear solution was cooled and then evaporated to dryness under reduced pressure. The obtained 1,2,3-triazole salt was suspended in 40 mL of acetonitrile, and 6-bromomethylcoumarin (2.95 g, 12.3 mmol) was added. The reaction mixture was stirred and heated under reflux for 7 days. After completion, the solvent was removed under reduced pressure, and the dry residue was repeatedly washed with hot acetonitrile (8 × 20 mL). The combined extracts were concentrated, and the residue was subjected to column chromatography (eluent: dichloromethane/acetonitrile, 10/0.9 v/v), affording 0.592 g of 6-(1,2,3-triazol-1-ylmethyl)coumarin (**L1**, yield: 21.2%) and 0.671 g of 6-(1,2,3-triazol-2-ylmethyl)coumarin (**L2**, yield: 24.0%).

Elemental analysis, found for **L1**: C, 63.2%; H, 4.2%; N, 18.4%.

Calculated for $C_{12}H_9N_3O_2$ (M = 227.22 g mol^{-1}): C, 63.4%; H, 4.0%; N, 18.5%.

^1H NMR for **L1** (500 MHz, CD_3CN) δ [ppm]: 5.62 (s, 2H), 6.40 (d, 1H, J = 9.6 Hz), 7.32 (d, 1H, J =8.4 Hz), 7.51 (m, 2H), 7.67 (s, 1H), 7.82 (d, 1H, J = 8.5 Hz), 8.83 (s, 1H).

^{13}C NMR for **L1** (500 MHz, CD_3CN) δ [ppm]: 53.4, 118.0, 120.3, 125.4, 128.7, 132.4, 133.3, 134.8, 144.4, 154.8, 161.2.

Elemental analysis, found for **L2**: C, 63.3%; H, 3.8%; N, 18.3%.

Calculated for $C_{12}H_9N_3O_2$ (M = 227.22 g mol^{-1}): C, 63.4%; H, 4.0%; N, 18.5%.

^1H NMR for **L2** (500 MHz, CD_3CN) δ [ppm]: 5.70 (s, 2H), 6.38 (d, 1H, J = 9.6 Hz), 7.16 (m, 1H), 7.18 (m, 1H), 7.57 (d, 1H, J = 7.9 Hz), 7.70 (s, 2H), 7.83 (d, 1H, J = 9.7 Hz).

^{13}C NMR for **L2** (500 MHz, CD_3CN) δ [ppm]: 58.4, 116.7, 117.7, 119.8, 124.8, 129.7, 135.9, 141.2, 144.3, 155.1, 161.2.

Synthesis of $[Fe(L1)_6](ClO_4)_2·2CH_3CN$(1)

The coordination compound **1** was obtained from the reaction of 6-(1,2,3-triazol-1-ylmethyl)coumarin (**L1**) with iron(II) perchlorate hexahydrate in a 6:1 molar ratio. 6-(1,2,3-triazol-1-ylmethyl)coumarin (32.4 mg, 0.143 mmol) was dissolve in 7 ml of dry, oxygen-free acetonitrile than $Fe(ClO_4)_2·6H_2O$ (8.63 mg, 0.0238 mmol) was added. The resulting colorless solution was left in a sealed Schlenk flask under a nitrogen atmosphere at room temperature. After 7 days, the compound crystallized as colorless crystals. Yield: 13.8 mg (34.1%).

Elemental analysis, found: C, 53.7%; H, 3.1%; N, 16.7%.

Calculated for $C_{76}H_{60}Cl_2FeN_{20}O_{20}$ (M = 1700.19 g mol^{-1}): C, 53.7%; H, 3.6%; N, 16.5%.

Synthesis of $[Fe(L1)_6](ClO_4)_2$ (2)

The coordination compound **2** is the product of a conversion process starting from compound **1**, whose crystals, when left in a Schlenk flask under a nitrogen atmosphere in the mother solution, gradually convert into compound **2**. The conversion begins after approximately two weeks and is complete after one and a half months.

Elemental analysis, found: C, 53.2%; H, 3.5%; N, 15.9%.

Calculated for $C_{72}H_{54}N_{18}O_{20}Cl_2Fe$ (M = 1618.08 g mol^{-1}): C, 53.4%; H, 3.4%; N, 15.6%.

Photoconversion 1 → 1c and 2 → 2c.

Macroscopic samples of **1c** and **2c** (20 mg) were obtained using Mössbauer spectroscopy monitoring, irradiating samples **1** and **2** respectively, from a distance 80 mm (λ = 365 nm, light power 10 mW according to optical power meter LM 2).

Contribution of product of photoconversion (dimer) in **1c** and **2c** in relation to remained ligand **L1** was besides single crystal X-ray diffraction studies, estimated also by ^{1}H NMR spectroscopy (see spectrum below). For this purpose, 4 mg of sample **1c** or **2c** was dissolved at room temperature in 0.5 ml of the mixture deuterated acetonitrile/deuterated water (20/1 v/v). The molar ratio of dimer (signals marked as "d" on spectrum) to monomer (signals marked as "m") was estimated to be 0.42:1 based on integration of signals of protons of methylene linkers (see ^{1}H NMR spectrum given below).

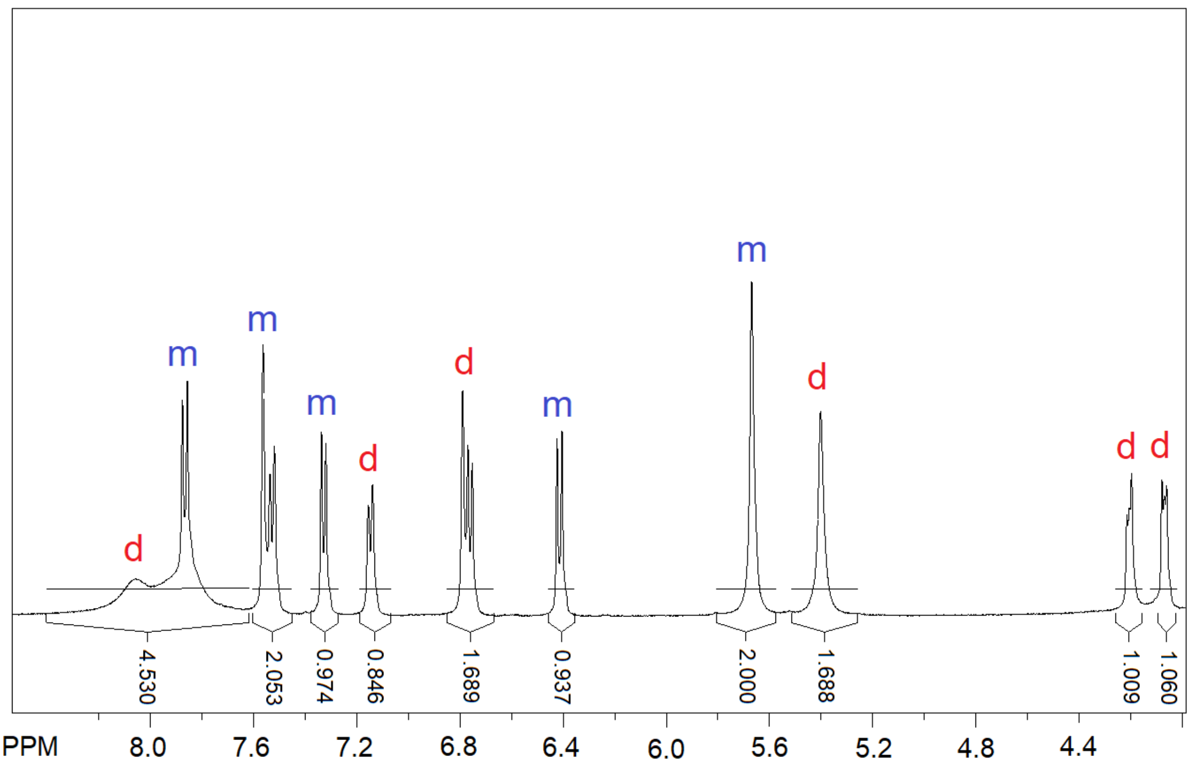

Molar ratio of dimer to monomer determined from ^{1}H NMR spectrum for **2c** equals 1.92:1, respectively (see below).

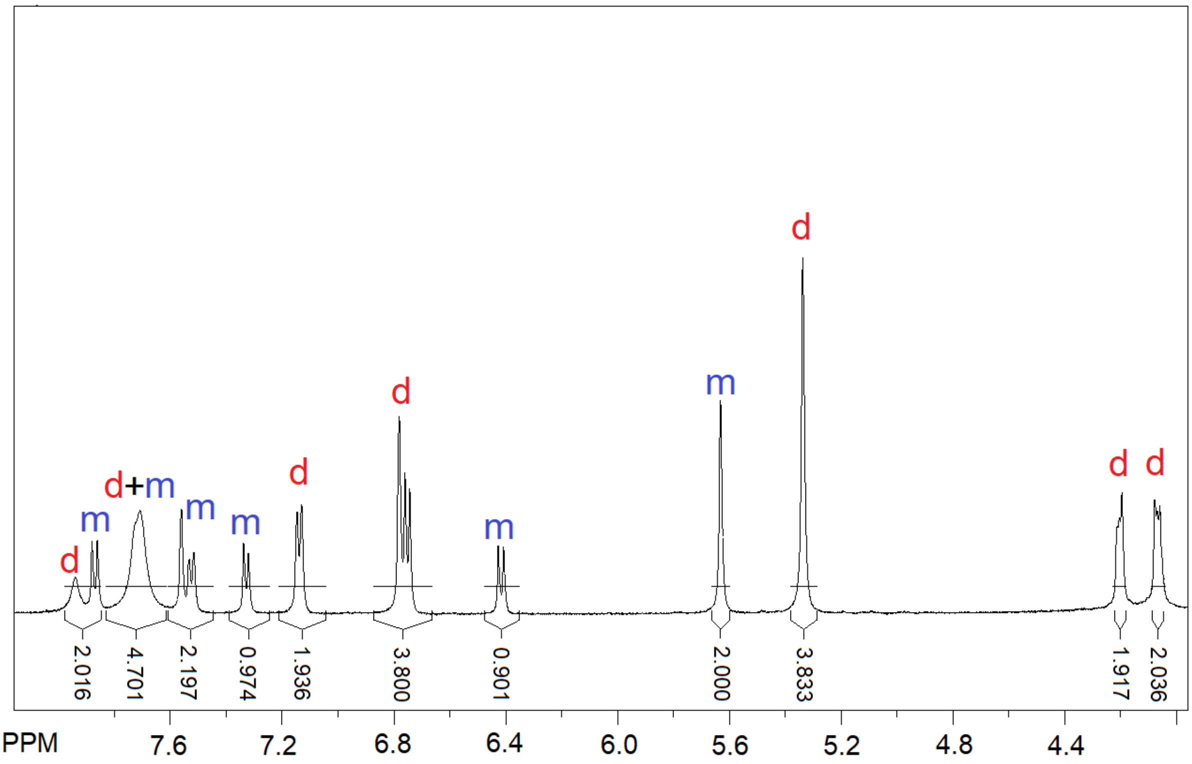

Table S1. Crystallographic data for crystal structures of **1** and **1c**.

CCDC no.	2490230	2490231	2490232	2490233
Compound	**1**	**1**	**1c**	**1c**
Molecular formula	$[Fe(C_{12}H_9N_3O_2)_6](ClO_4)_2\cdot 2CH_3CN$	$[Fe(C_{12}H_9N_3O_2)_6](ClO_4)_2\cdot 2CH_3CN$	$[Fe(C_{12}H_9N_3O_2)_6](ClO_4)_2\cdot 2CH_3CN$	$[Fe(C_{12}H_9N_3O_2)_6](ClO_4)_2\cdot 2CH_3CN$
Empirical formula	$C_{76}H_{60}Cl_2FeN_{20}O_{20}$	$C_{76}H_{60}Cl_2FeN_{20}O_{20}$	$C_{76}H_{60}Cl_2FeN_{20}O_{20}$	$C_{76}H_{60}Cl_2FeN_{20}O_{20}$
Formula weight	1700.19	1700.19	1700.19	1700.19
Temperature / K	**250**	**80**	**250**	**80**
Spin state	**HS**	**LS**	**HS**	**LS**
Crystal system	orthorhombic	orthorhombic	orthorhombic	orthorhombic
Space group	*Pbcn*	*Pbcn*	*Pbcn*	*Pbcn*
a / Å	41.471(12)	41.017(10)	41.133(10)	40.716(10)
b / Å	11.309(4)	11.019(2)	11.274(3)	11.004(2)
c / Å	16.503(5)	16.381(3)	16.609(4)	16.499(3)
α /°	90	90	90	90
β /°	90	90	90	90
γ /°	90	90	90	90
Volume / Å^3	7740(4)	7404(3)	7702(3)	7392(3)
Z	4	4	4	4
ρ_{calc} / g cm^{-3}	1.459	1.525	1.466	1.528
μ/mm^{-1}	0.351	0.367	0.353	0.368
F(000)	3504.0	3504.0	3504.0	3504.0
Crystal size / mm^3	0.36 × 0.11 × 0.04	0.36 × 0.11 × 0.04	0.75 × 0.19 × 0.07	0.75 × 0.19 × 0.07
Radiation	MoKα (λ = 0.71073)	MoKα (λ = 0.71073)	Mo Kα (λ = 0.71073)	Mo Kα (λ = 0.71073)
2Θ range for data collection / °	4.476 to 52.744	3.972 to 52.044	4.478 to 52.744	4.56 to 50.05
Index ranges	$-51 \le h \le 51$ $-14 \le k \le 14$ $-20 \le l \le 20$	$-50 \le h \le 50$ $-13 \le k \le 13$ $-20 \le l \le 20$	$-51 \le h \le 51$ $-14 \le k \le 14$ $-20 \le l \le 20$	$-48 \le h \le 46$ $-13 \le k \le 13$ $-19 \le l \le 19$
Reflections collected	41877	37940	84492	65484
Independent reflections	7905 [R_{int} = 0.0315, R_{sigma} = 0.0226]	7296 [R_{int} = 0.0284, R_{sigma} = 0.0195]	7867 [R_{int} = 0.0489, R_{sigma} = 0.0217]	6532 [R_{int} = 0.0481, R_{sigma} = 0.0200]
Data/restraints/parameters	7905/10/554	7296/0/538	7867/388/681	6532/336/620
Goodness-of-fit on F^2	1.026	1.137	1.140	1.327
Final R indexes [I>=2σ (I)]	R_1 = 0.0390, wR_2 = 0.0987	R_1 = 0.0427, wR_2 = 0.0956	R_1 = 0.0684, wR_2 = 0.1593	R_1 = 0.0992, wR_2 = 0.1979
Final R indexes [all data]	R_1 = 0.0536, wR_2 = 0.1062	R_1 = 0.0501, wR_2 = 0.0986	R_1 = 0.0840, wR_2 = 0.1668	R_1 = 0.1022, wR_2 = 0.1989
Largest diff. peak/hole / e Å^{-3}	0.36/-0.36	0.40/-0.51	0.56/-0.46	0.71/-0.56

Table S2. Crystallographic data for crystal structures of **2** and **2c**.

CCDC no.	2490226	2490227	2490228	2490229
Compound	**2**	**2**	**2c**	**2c**
Molecular formula	$[Fe(C_{12}H_9N_3O_2)_6](ClO_4)_2$	$[Fe(C_{12}H_9N_3O_2)_6](ClO_4)_2$	$[Fe(C_{12}H_9N_3O_2)_6](ClO_4)_2$	$[Fe(C_{12}H_9N_3O_2)_6](ClO_4)_2$
Empirical formula	$C_{72}H_{54}N_{18}O_{20}Cl_2Fe$	$C_{72}H_{54}N_{18}O_{20}Cl_2Fe$	$C_{72}H_{54}N_{18}O_{20}Cl_2Fe$	$C_{72}H_{54}N_{18}O_{20}Cl_2Fe$
Formula weight	1618.08	1618.08	1618.08	1618.08
Temperature / K	**250**	**80**	**300**	**80**
Spin state	**HS**	**50% LS**	**HS**	**LS**
Crystal system	monoclinic	monoclinic	monoclinic	monoclinic
Space group	$P2_1/c$	$P2_1/c$	$P2_1/c$	$P2_1/c$
a / Å	18.120(4)	18.070(11)	18.008(2)	17.714(2)
b / Å	8.792(2)	8.739(3)	8.733(1)	8.679(1)
c / Å	22.170(5)	21.758(7)	22.350(3)	21.808(4)
α /°	90	90	90	90
β /°	100.14(2)	100.542(4)	91.89(1)	91.94(1)
γ /°	90	90	90	90
Volume / Å^3	3476.8(14)	3378(3)	3512.9(7)	3350.8(8)
Z	2	2	2	2
ρ_{calc} / g cm^{-3}	1.546	1.591	1.530	1.604
μ/mm^{-1}	0.386	0.397	0.382	0.401
F(000)	1664.0	1664.0	1664.0	1664.0
Crystal size / mm^3	0.38 × 0.20 × 0.08	0.38 × 0.20 × 0.08	0.48 × 0.45 × 0.22	0.48 × 0.45 × 0.22
Radiation	Mo Kα (λ = 0.71073)	Mo Kα (λ = 0.71073)	Mo Kα (λ = 0.71073)	Mo Kα (λ = 0.71073)
2Θ range for data collection / °	4.568 to 61.01	4.07 to 61.444	4.526 to 57.4	4.454 to 61.996
Index ranges	$-25 \le h \le 25$ $-12 \le k \le 12$ $-31 \le l \le 29$	$-19 \le h \le 24$ $-12 \le k \le 10$ $-29 \le l \le 30$	$-24 \le h \le 24$ $-11 \le k \le 11$ $-27 \le l \le 30$	$-25 \le h \le 25$ $-12 \le k \le 12$ $-31 \le l \le 30$
Reflections collected	52031	20478	204161	113732
Independent reflections	10594 [R_{int} = 0.0303, R_{sigma} = 0.0235]	9637 [R_{int} = 0.0523, R_{sigma} = 0.0973]	9058 [R_{int} = 0.0341, R_{sigma} = 0.0100]	10681 [R_{int} = 0.0432, R_{sigma} = 0.0215]
Data/restraints/parameters	10594/0/511	9637/0/511	9058/0/548	10681/0/539
Goodness-of-fit on F^2	1.032	1.014	1.040	1.043
Final R indexes [I>=2σ (I)]	R_1 = 0.0415, wR_2 = 0.1073	R_1 = 0.0627, wR_2 = 0.1084	R_1 = 0.0410, wR_2 = 0.1134	R_1 = 0.0379, wR_2 = 0.0958
Final R indexes [all data]	R_1 = 0.0556, wR_2 = 0.1142	R_1 = 0.1227, wR_2 = 0.1314	R_1 = 0.0465, wR_2 = 0.1175	R_1 = 0.0439, wR_2 = 0.0986
Largest diff. peak/hole / e Å^{-3}	0.38/-0.46	0.56/-0.62	0.26/-0.39	0.49/-0.51

Table S2 continued. Crystallographic data for crystal structure of **2c** heated at 230°C .

CCDC no.	2490234
Compound	**2c - after_heating to 503 K**
Molecular formula	$[Fe(C_{12}H_9N_3O_2)_6](ClO_4)_2$
Empirical formula	$C_{72}H_{54}N_{18}O_{20}Cl_2Fe$
Formula weight	1618.08
Temperature / K	120(1)
Spin state	**LS**
Crystal system	monoclinic
Space group	$P2_1/c$
a / Å	17.766(5)
b / Å	8.693(4)
c / Å	21.924(6)
α /°	90
β /°	92.11(3)
γ /°	90
Volume / Å^3	3384(2)
Z	2
ρ_{calc} / g cm^{-3}	1.588
μ/mm^{-1}	3.321
F(000)	1664.0
Crystal size / mm^3	0.22 × 0.17 × 0.12
Radiation	Cu Kα (λ = 1.54184)
2Θ range for data collection / °	4.978 to 148.772
Index ranges	$-22 \leq h \leq 22$ $-10 \leq k \leq 10$ $-22 \leq l \leq 27$
Reflections collected	42233
Independent reflections	6732 [R_{int} = 0.0478, R_{sigma} = 0.0403]
Data/restraints/parameters	6732/14/576
Goodness-of-fit on F^2	1.046
Final R indexes [I>=2σ (I)]	R_1 = 0.0476, wR_2 = 0.1062
Final R indexes [all data]	R_1 = 0.0721, wR_2 = 0.1180
Largest diff. peak/hole / e Å^{-3}	0.28/-0.47

Table S3. Values of torsion angles involving the methylene group in the initial compound (**2**) and the photoconversion product (**2c**).

Torsion angles	2 (250 K)	2c (300 K)
N5 - N4 - C22 - C18	-79.6(2)	-89.4(2)
C23 - N4 - C22 - C18	96.2(2)	91.8(2)
C17 - C18 - C22 - N4	-86.5(2)	-111.2(2)
C19 - C18 - C22 - N4	90.9(2)	70.2(2)
N8 - N7 - C34 - C30	90.2 (2)	86.4(2)
C35 - N7 - C34 - C30	-92.6(2)	-96.3(2)
C29 - C30 - C34 - N7	-19.8(2)	-6.4(3)
C31 - C30 - C34 - N7	162.5(1)	173.7(2)

Table S4. Values of torsion angles N-Fe-N—C(triazole) for compounds: **1**, **1c** (a) and **2, 2c** (b).

a)

Torsion angles	**1 (HS, 250 K)**	**1 (LS, 80 K)**	**1c (HS, 250 K)**	**1c (LS, 80 K)**
N3 - Fe1 - N6 - C24	-46.38(18)	-50.63(18)	-48.15(31)	-51.75(50)
N3 - Fe1 - N9 - C36	126.95(17)	129.28(17)	126.09(29)	128.45 (0.47)
N6 - Fe1 - N3 - C12	-51.85(16)	-43.13(17)	-52.06(27)	-43.98 (0.45)
N6 - Fe1 - N9 - C36	22.21(1.58)	61.16(2.37)	7.32(2.86)	44.52 (7.02)
N9 - Fe1 - N3 - C12	130.32(16)	138.45(17)	129.84(27)	137.62 (0.45)
N9 - Fe1 - N6 - C24	58.42 (1.56)	17.53(2.42)	70.68(2.78)	32.21 (7.08)

b)

Torsion angles	**2 (HS, 250 K)**	**2 (LS, 80 K)**	**2c (HS, 300 K)**	**2c (LS, 80 K)**
N3 - Fe1 - N6 - C24	47.96 (15)	48.10(25)	52.09(16)	50.67(11)
N3 - Fe1 - N9 - C36	119.06 (14)	120.23(24)	128.50(15)	130.03(11)
N6 - Fe1 - N3 - C12	61.12 (13)	58.86(23)	60.18(15)	52.57(10)
N6 - Fe1 - N9 - C36	31.25 (14)	32.59(24)	41.14(15)	42.70(11)
N9 - Fe1 - N3 - C12	-29.77 (13)	-32.42(22)	-32.48(15)	-39.92(10)
N9 - Fe1 - N6 - C24	136.89 (14)	136.64(25)	139.84(16)	138.15(11)

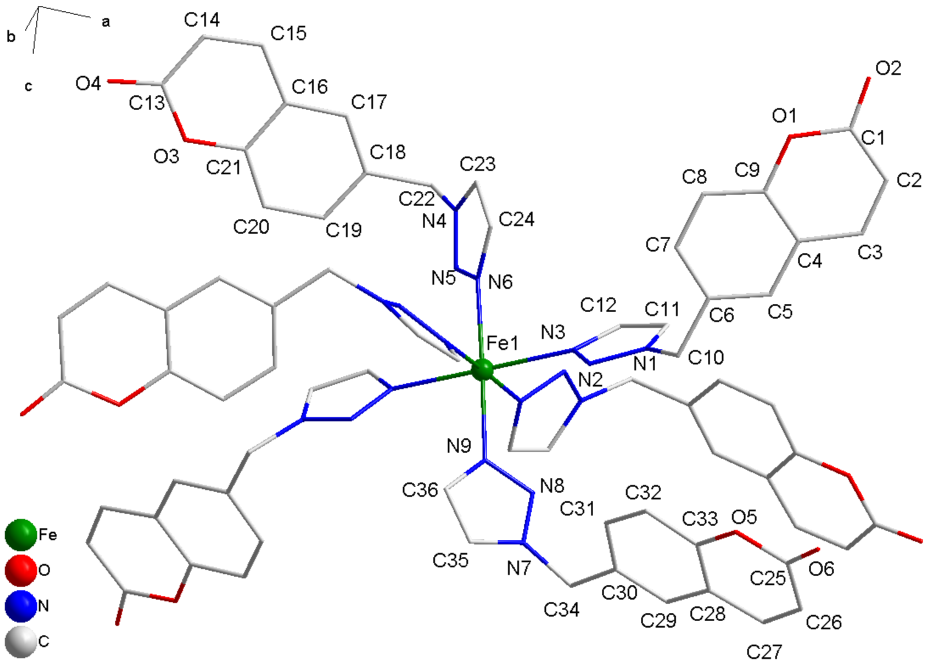

Figure S1. The coordination environment of Fe(II) together with atom labels (crystallographically independent part) in **1**.

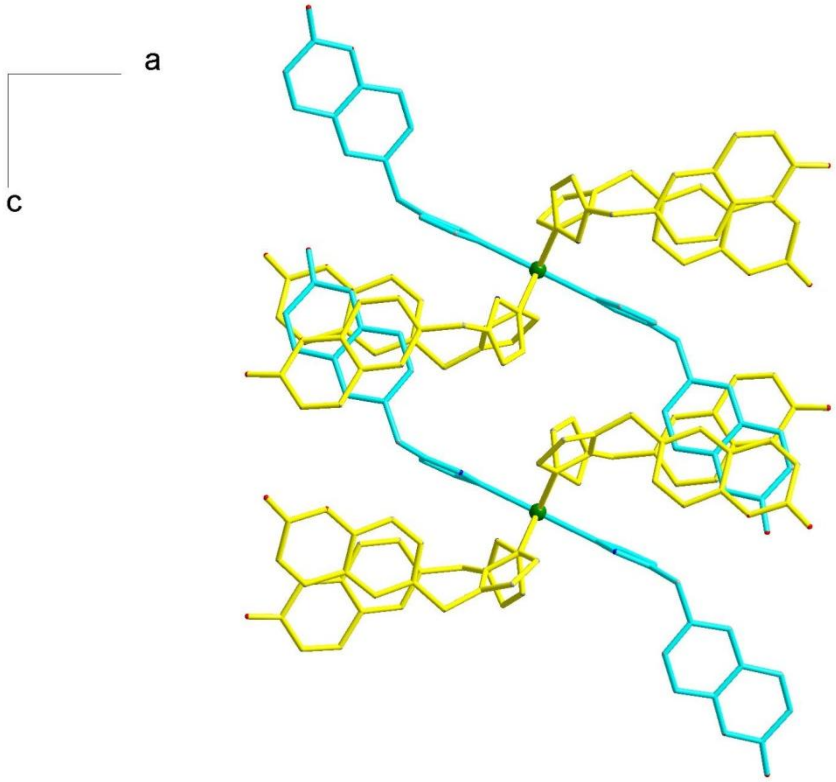

Figure S2. Overlapping of coumarin fragments in **1**. Turquoise color indicates molecules directed into neighboring columns.

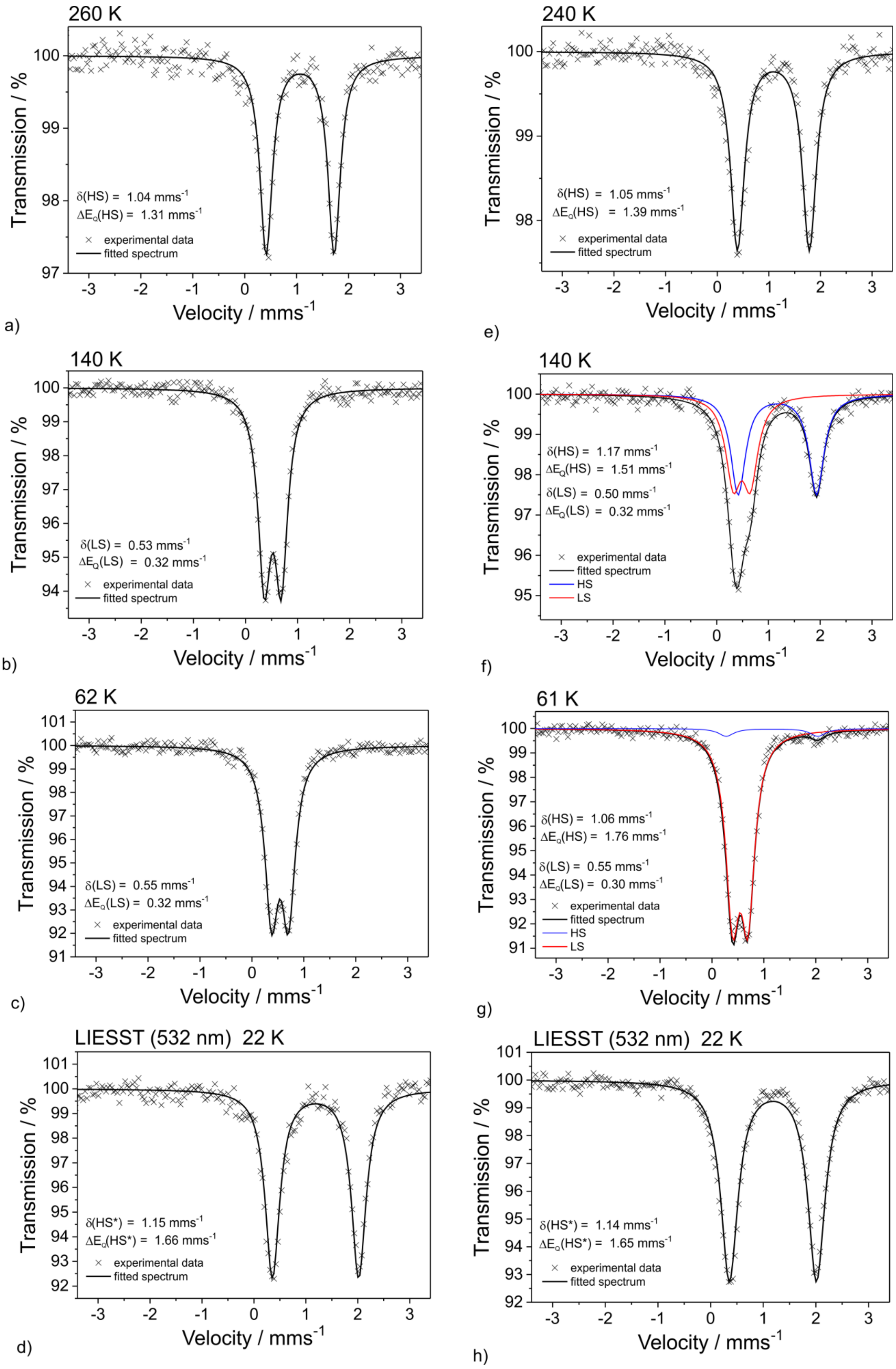

Figure S3. Mössbauer spectra for **1** (left column) and **1c** (right column).

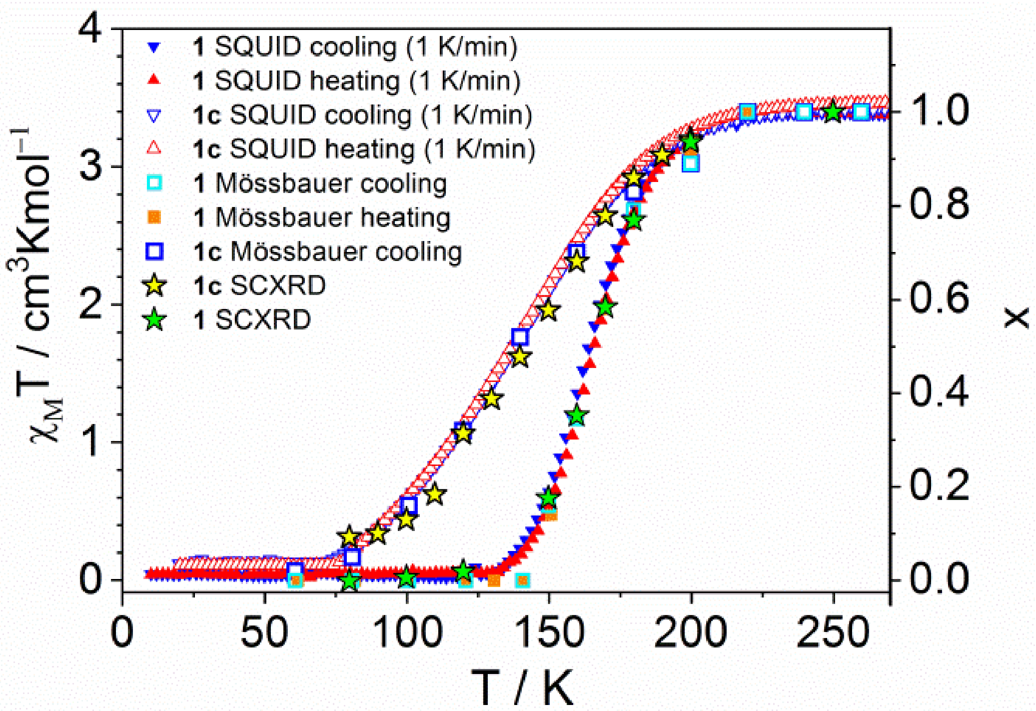

Figure S4. Temperature dependences of $\chi_M T$ (SQUID), relative areas of HS form derived from Mössbauer spectroscopy and from single crystal X-ray diffraction studies for **1** (a) and **1c** (b). x was defined for Mössbauer spectroscopy according to $A_{HS}/(A_{HS} + A_{LS})$ whereas for SCXRD as $(d_{Fe\text{-}N}{}^{T} - d_{Fe\text{-}N}{}^{LS})/(d_{Fe\text{-}N}{}^{HS} - d_{Fe\text{-}N}{}^{LS})$ where d is average Fe-N distance determined at temperature T, for HS and for LS form. $d_{Fe\text{-}N}{}^{LS}$ was estimated taking into account that at 80 K the contribution of HS form equals to 0.05 according to Mössbauer spectroscopy.

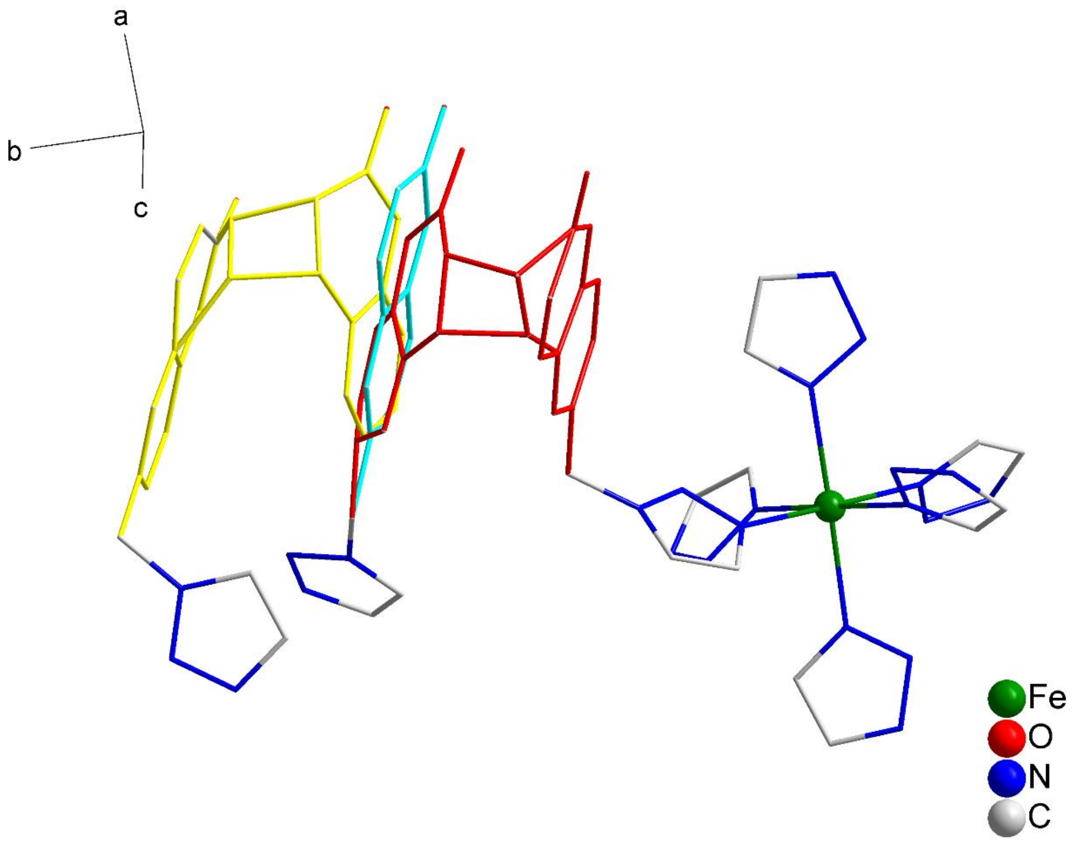

Figure S5. The coordination environment of Fe(II) and structure of dimerized ligands in **1c**.

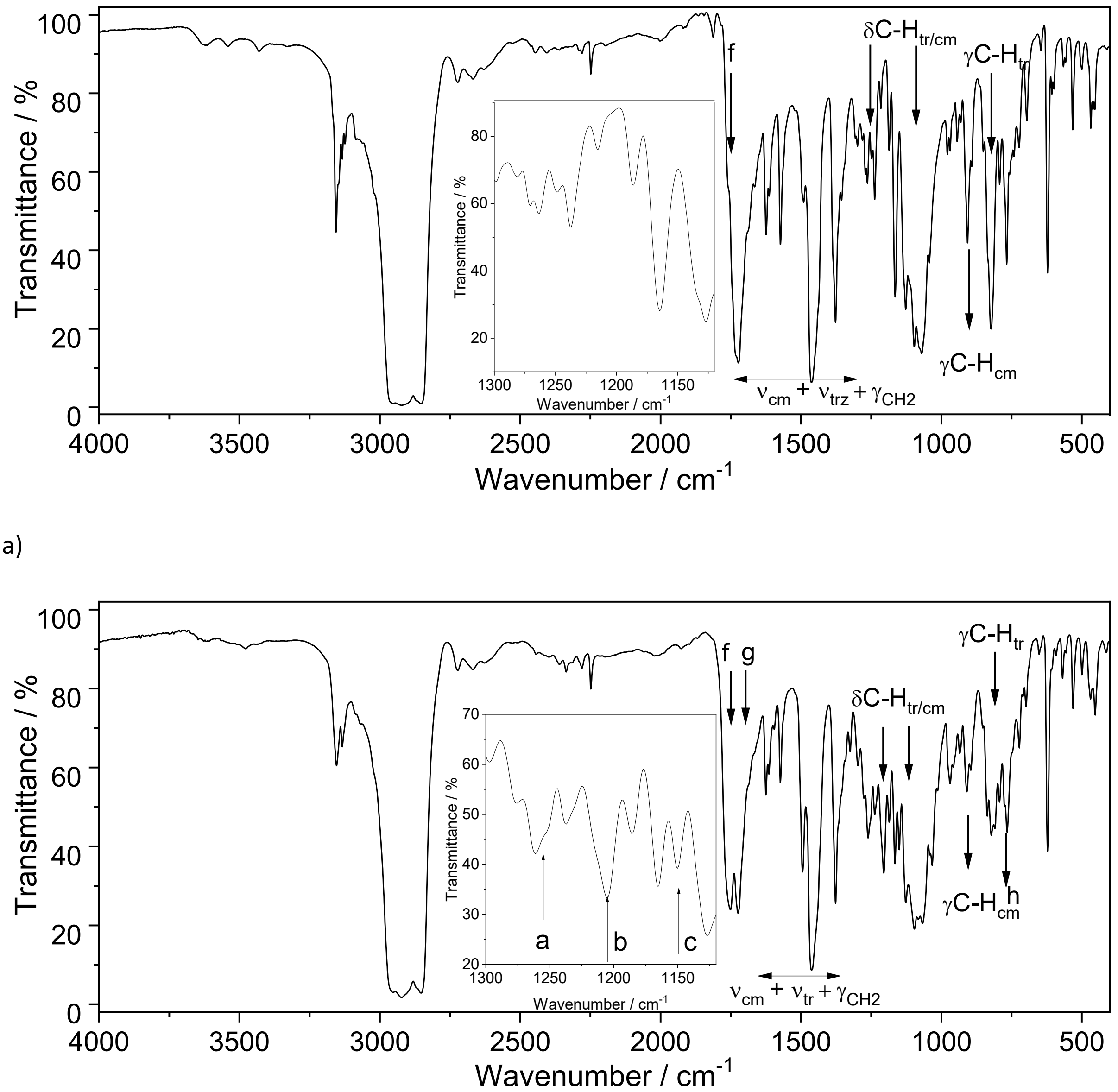

Figure S6. IR spectra of **1** (top) and **1c** in Nujol with the band assignments. The notation a-c, f and g is the same as in Fig.3 in main text. The appearance of the new peak at 760 cm^{-1} after fotoconversion corresponds to the band due to puckering of the cyclobutane fragment as shown by the DFT calculations (calculated value of 750 cm^{-1}). Note the presence of MeCN bands at ca. 2250 cm^{-1}.

Comment to LIESST and r-LIESST experiments in 1 and 1c

A sample of compound **1** was cooled to 10 K (1 K min^{-1}) and then irradiated with light of a wavelength of 532 nm to reach signal saturation (Fig. S4a) corresponding to a quantitative switch to the metastable high-spin form. Then the light was turned off and temperature was elevated 0.3 K min^{-1}. Above 30 K fast relaxation to LS form occurs (T_{LIESST} = 35 K). A sample of compound **1** was cooled again to 10 K (1 K min^{-1}) and switched to the high-spin form with 532 nm light. Then the heating cycle was started with the light source turned on (LITH, Fig. S4b). After reaching the temperature of 90 K, the measurement in the cooling mode was started.

LIESST (Fig. S4c) and LITH (Fig. S4d) experiments for **1c** were performed in the same manner as for sample **1**.

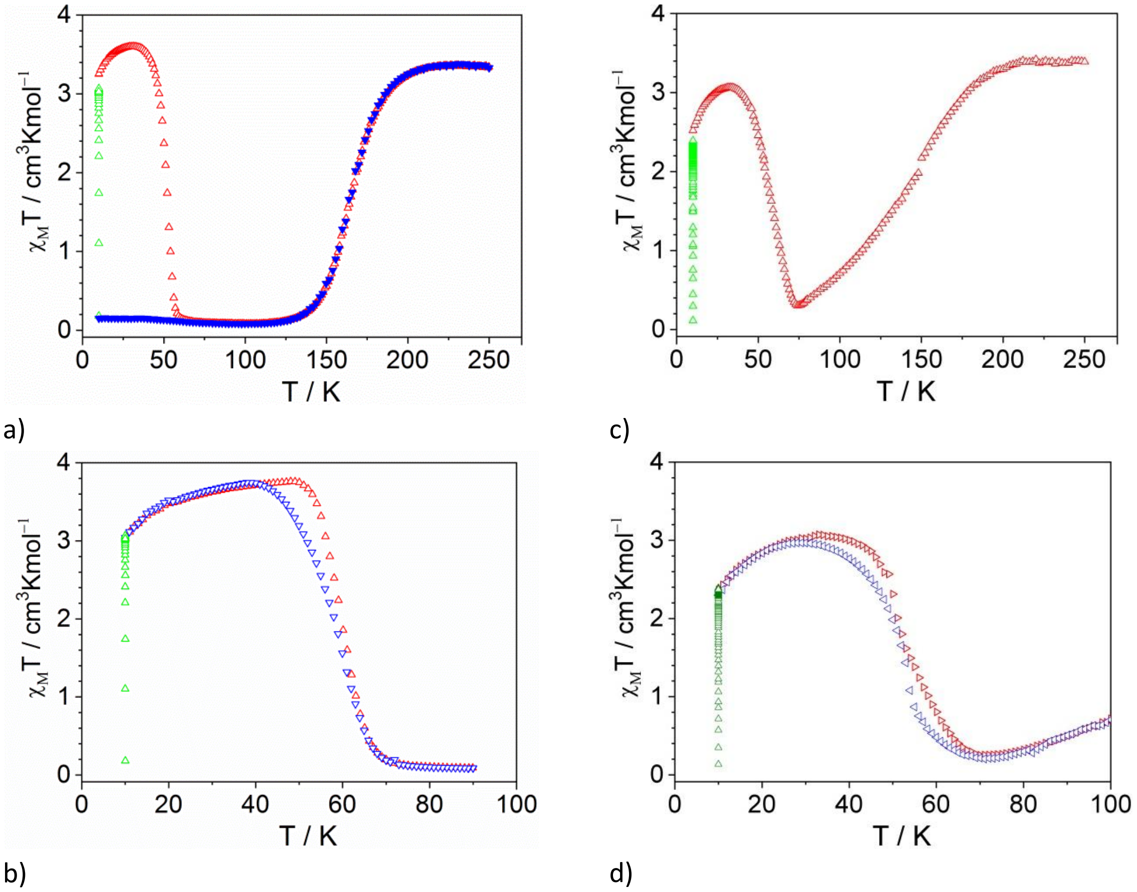

Figure S7. $\chi_M T(T)$ dependences recorded for LIESST (upper row) and LITH (bottom row) experiments for **1** (a, b) and **1c** (c, d).

Comment to LIESST and r-LIESST experiments in 2

A sample of compound **2** was cooled to 60 K at a rate of 1 K min^{-1} and left at this temperature until the system reached a low-spin state (Fig. S7a). Then the sample was cooled (1 K min^{-1}) to 10 K. Irradiation with light of a wavelength of 532 nm leads to signal saturation, practically obtaining a quantitative switch to the metastable high-spin form. The laser has been turned off. The temperature was increased (0.3 K min^{-1}). Above 60 K the system relaxes to the LS form (T_{LIEEST} = 65 K), however after reaching 70 K the magnetic susceptibility increases again, covering the dependences for the first step of the spin transition.

In the next experiment (Fig. S7b), the sample was cooled to 10 K (1 K min^{-1}) by converting half of the Fe(II) ions to the LS form. By exposing the sample to 532 nm light, a switch was made to the HS* form. With the laser still on, heating was started (0.3 K min^{-1}, LITH). A very similar $\chi_M T(T)$ curve was obtained as in the LIESST experiment – above 60 K, relaxation to the LS state begins, but after reaching 75 K, the $\chi_M T(T)$ curve begins to overlap with the curve of the first stage of the spin crossover. After reaching 90 K, cooling of the sample was started (0.3 K min^{-1}). The $\chi_M T(T)$ dependence in the heating mode is very similar with the one obtained during cooling. It is worth noting that at 60-65 K a small perturbation appeared, which corresponds to the temperature at which the second step of the thermally induced spin crossover starts.

In the third experiment (Fig. S7c) we checked the possibility of performing the r-LIESST experiment. The sample was cooled to a temperature of 10 K (1 K min^{-1}). Then it was irradiated with green light (532 nm) until the signal was saturated, after which the sample was irradiated with 808 nm light to switch to the LS form. The value of $\chi_M T$ = 0.6 cm^3 K mol^{-1} was obtained, which corresponds to the contribution of HS form χ_{HS} = 0.17. Heating the sample (0.3 K min^{-1}) leads to a decrease in the value of $\chi_M T$ at a temperature above 50 K, after which it starts to grow, overlapping with the curve of the thermally induced spin crossover.

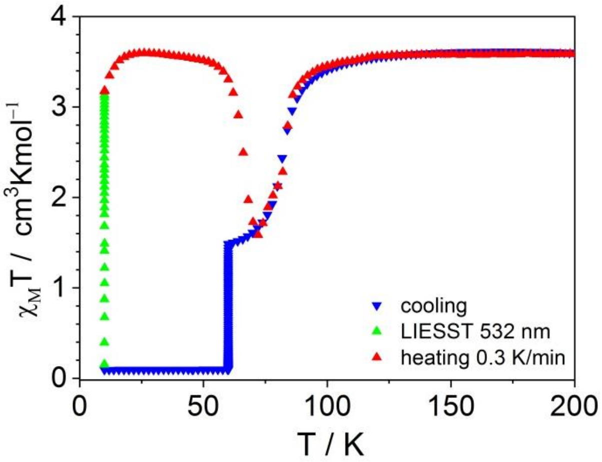

a)

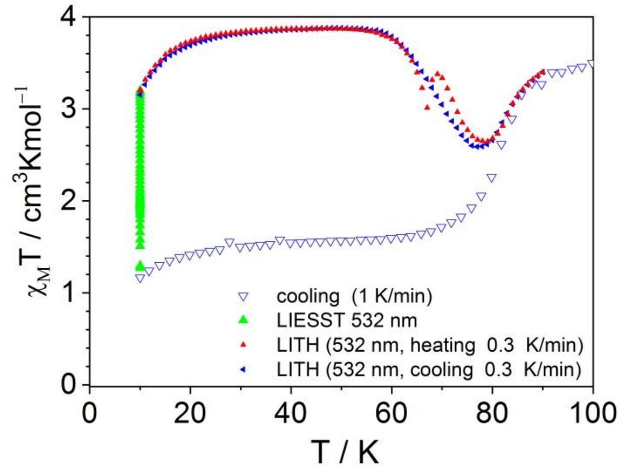

b)

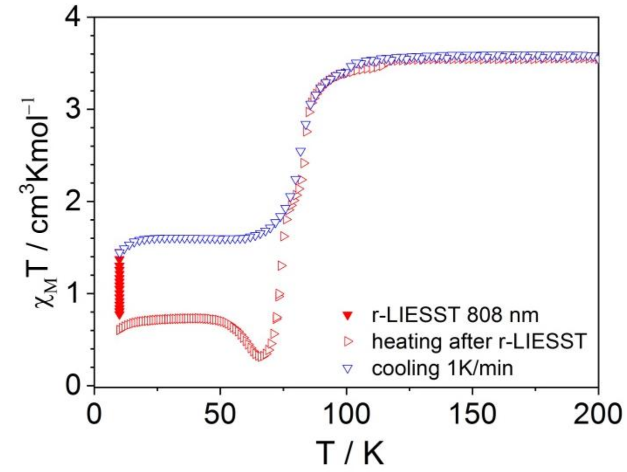

c)

Figure S8. χ_MT(T) dependences recorded for LIESST (a), LITH (b) and r-LIESST (c) experiments for **2**.

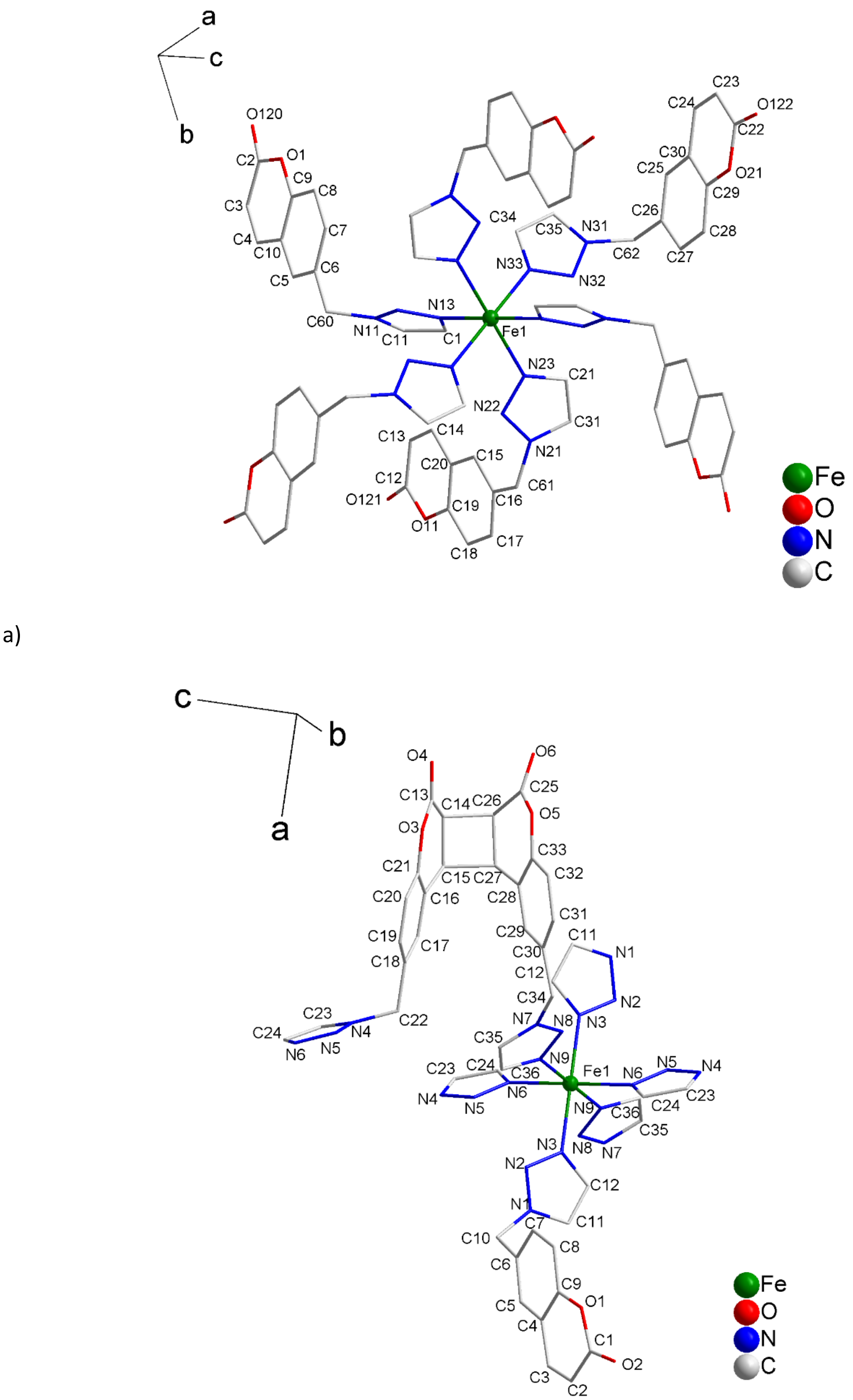

Figure S9. The coordination environment of Fe(II) together with atom labels (crystallographically independent part) in **2** (a) and **2c** (b).

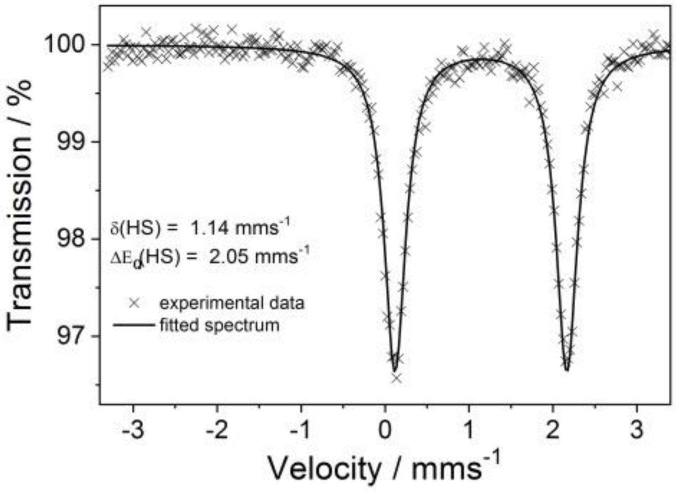

a)

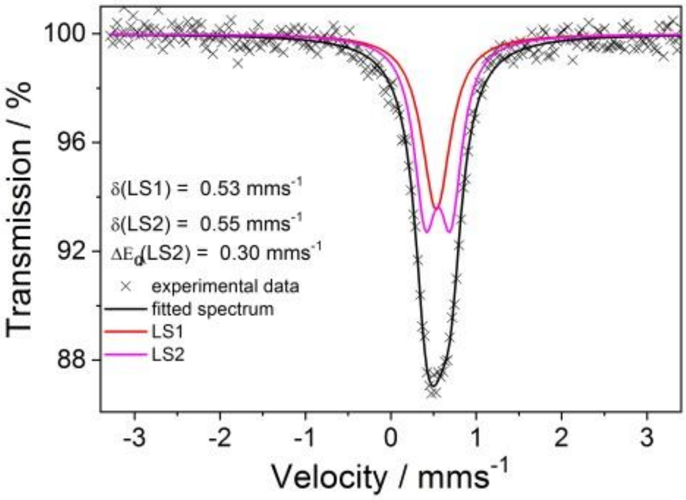

b)

Figure S10. Mössbauer spectra for **2** at 200 K (a) and 48 K (b).

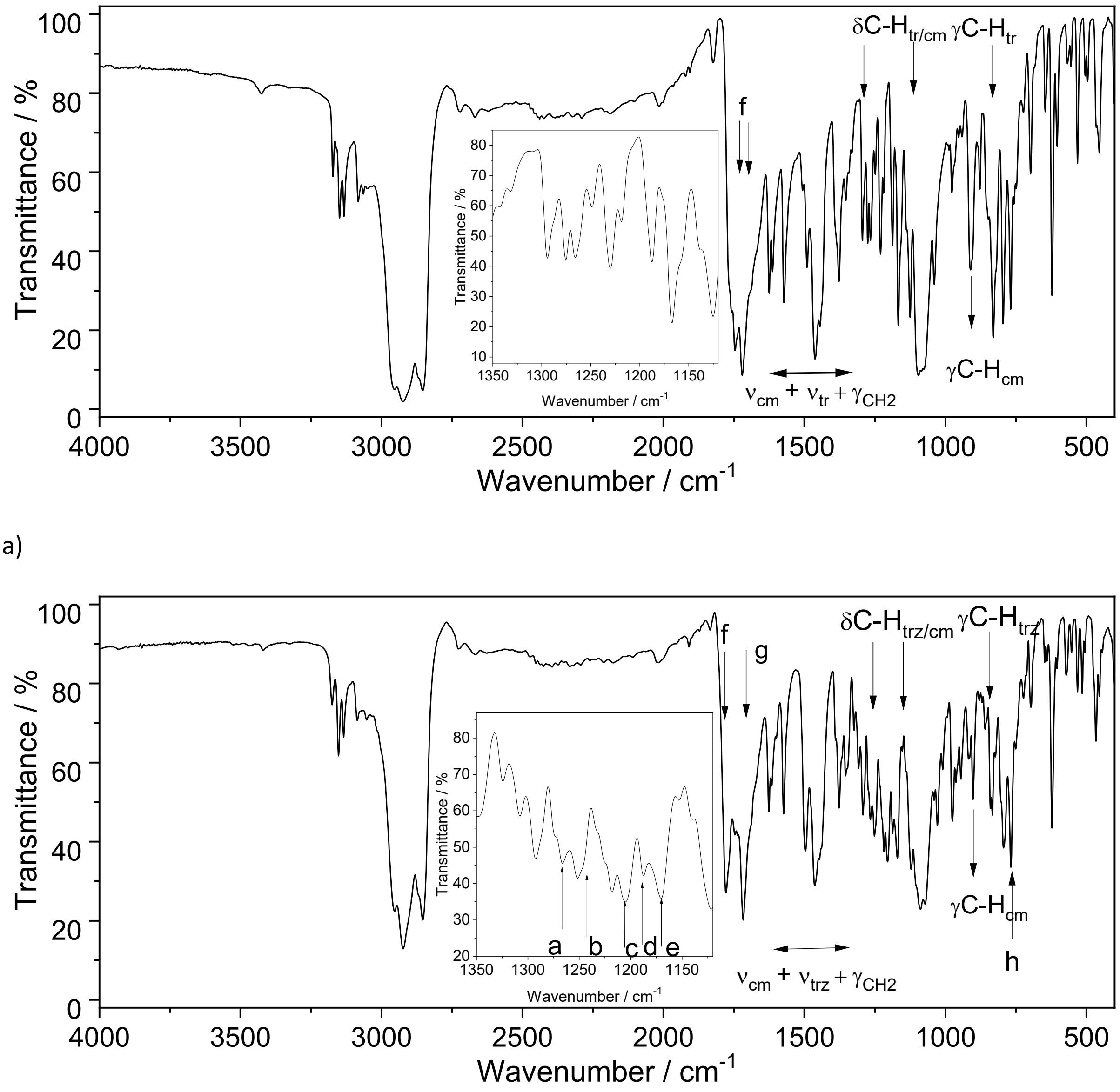

a)

b)

Figure S11. IR spectra of **2** (top) and **2c** in Nujol with the band assignments. The notation a-c, f and g is the same as in Fig.3 in main text. Again the appearence of the new peak at 760 cm^{-1} after fotoconversion corresponds to the band due to puckering of the cyclobutane fragment as shown by the DFT calculations (calculated value of 750 cm^{-1}). Note the lack of MeCN bands at ca. 2250 cm^{-1}.

Comment on the analysis of structural changes induced by the [2+2] photocycloaddition leading to cyclobutene ring formation

The dimerized ligand molecule in the photoconversion product **2c** is subjected to strong internal strain. This observation was confirmed by analyzing the puckering angles, which serve as a measure of distortion in alicyclic rings. For compound **2c**, the puckering angle is 11.8° at 300 K and 12.4°at 80 K (defined by the planes formed by atoms C14–C15–C27 and C14–C26–C27, Fig. S11a), whereas in previous shown tetrazole based compound,[7] this angle was 18.7° at 250 K and 19.2° at 80 K (between corresponding planes formed by atoms C13–C2–C3 and C13–C14–C3, Fig. S11b). Undoubtedly, in compound **2c**, the dimerized form of the ligand is subjected to much greater strain.

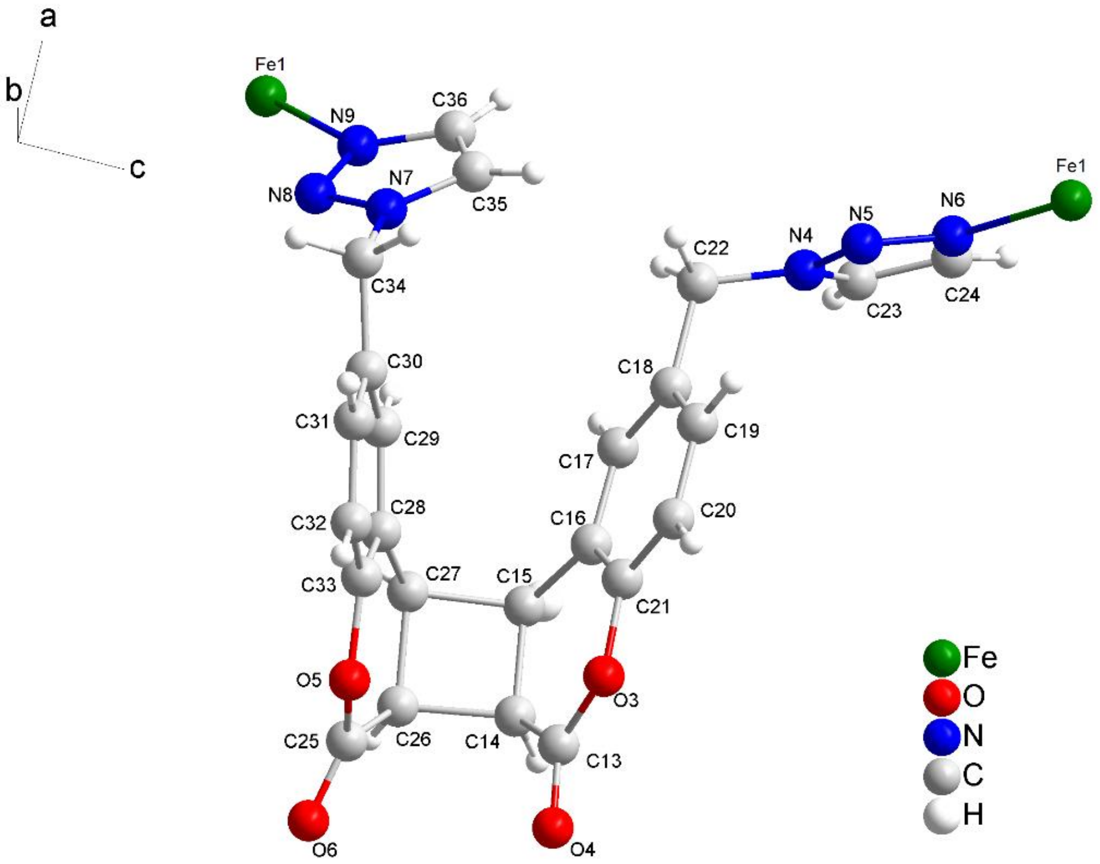

a)

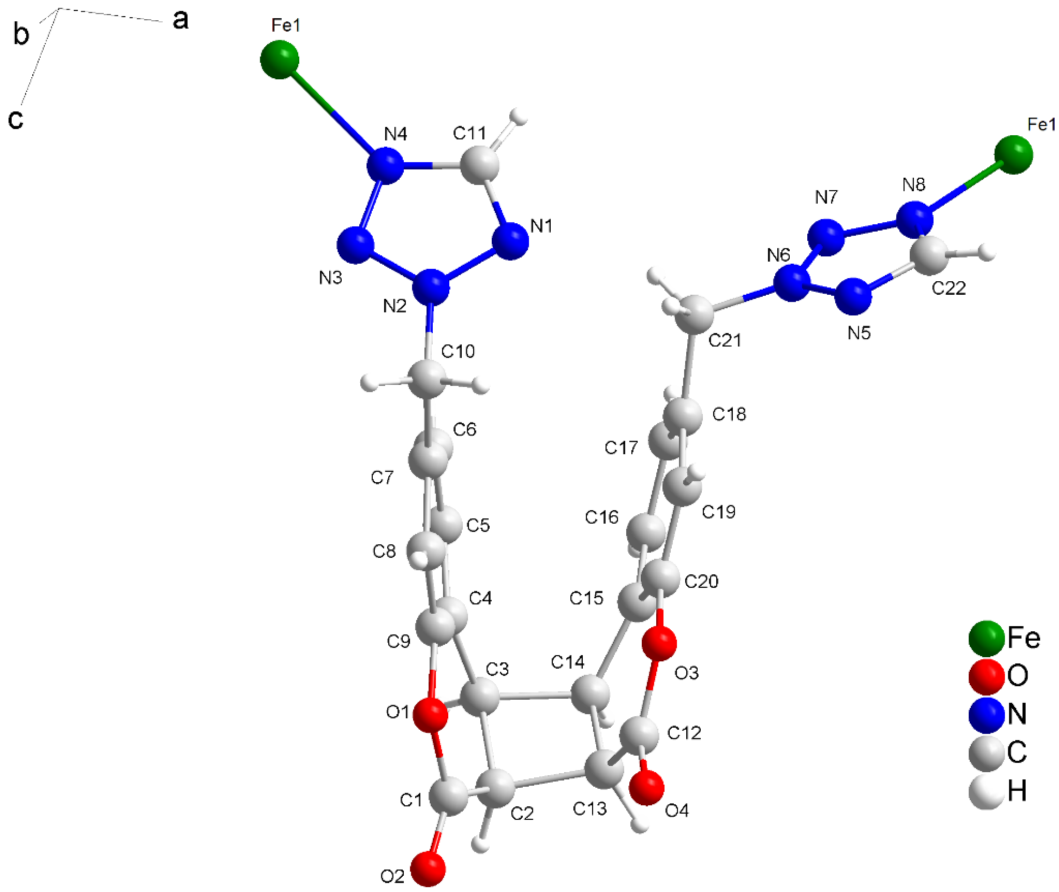

b)

Figure S12. Structure of the ligand in its dimeric form in coordination compounds obtained through the [2+2] cycloaddition reaction for compounds: tetrazole analogue (a) and **2c** (b).

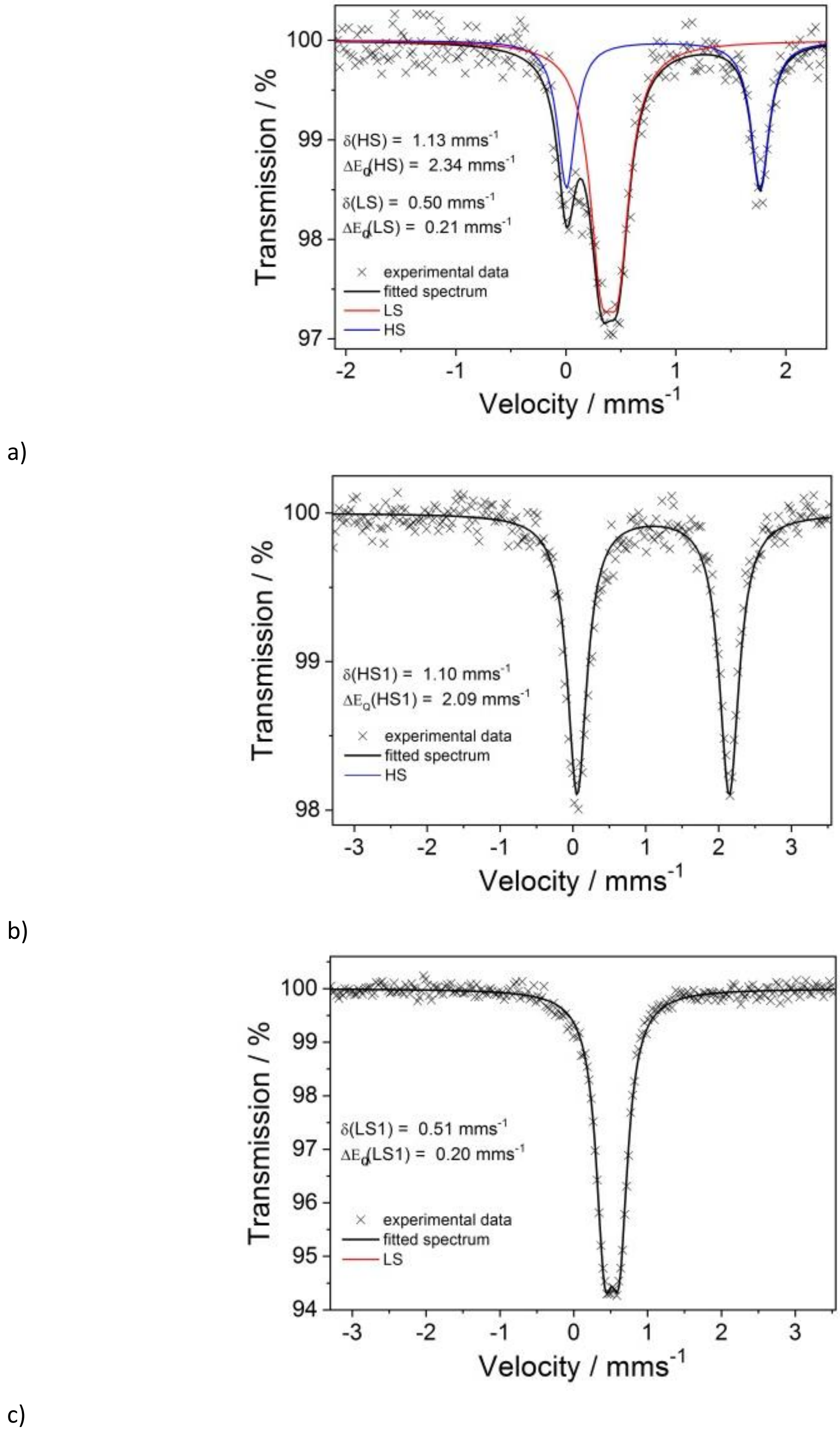

Figure S13. Mössbauer spectra showing photoconversion **2** → **2c** at 140 K (a) as well as spectra of **2c** recorded at 250 K (b) and 140 K (c).

Comment to LIESST and r-LIESST experiments 2c

2c was cooled to 10 K (1 K min^{-1}). Irradiation (532 nm) was carried out to reach signal saturation. and (Fig. S10a). When the light is turned off, a rapid relaxation during heating (0.3 K min^{-1}) to a low-spin form begins immediately. After the experiment was completed, the sample was cooled again to 10 K and irradiated (532 nm) with light until signal saturation was achieved. With the light on, a heating cycle to 70 K and then cooling to 10 K was performed (Fig. S10b).

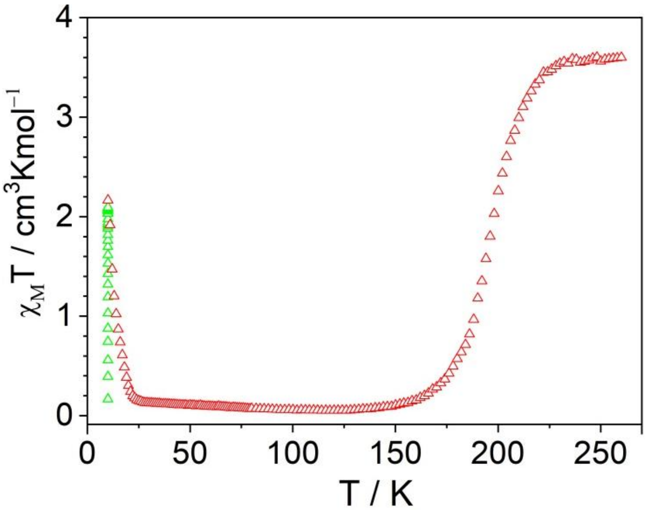

a)

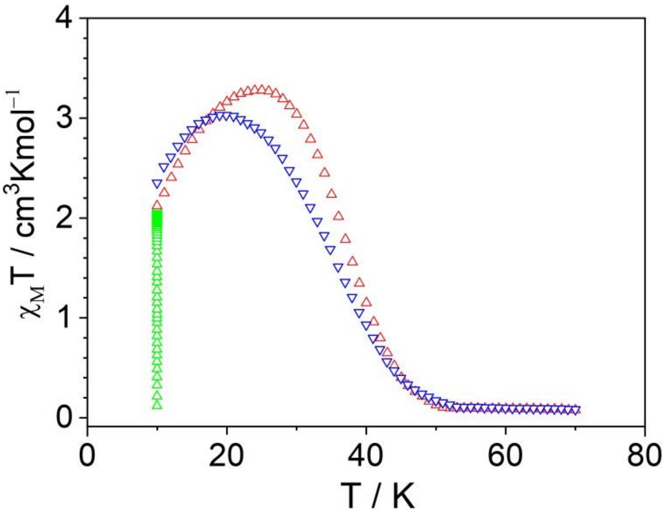

b)

Figure S14. χ_MT(T) dependences recorded for LIESST (a) and LITH (b) experiments for **2c**.

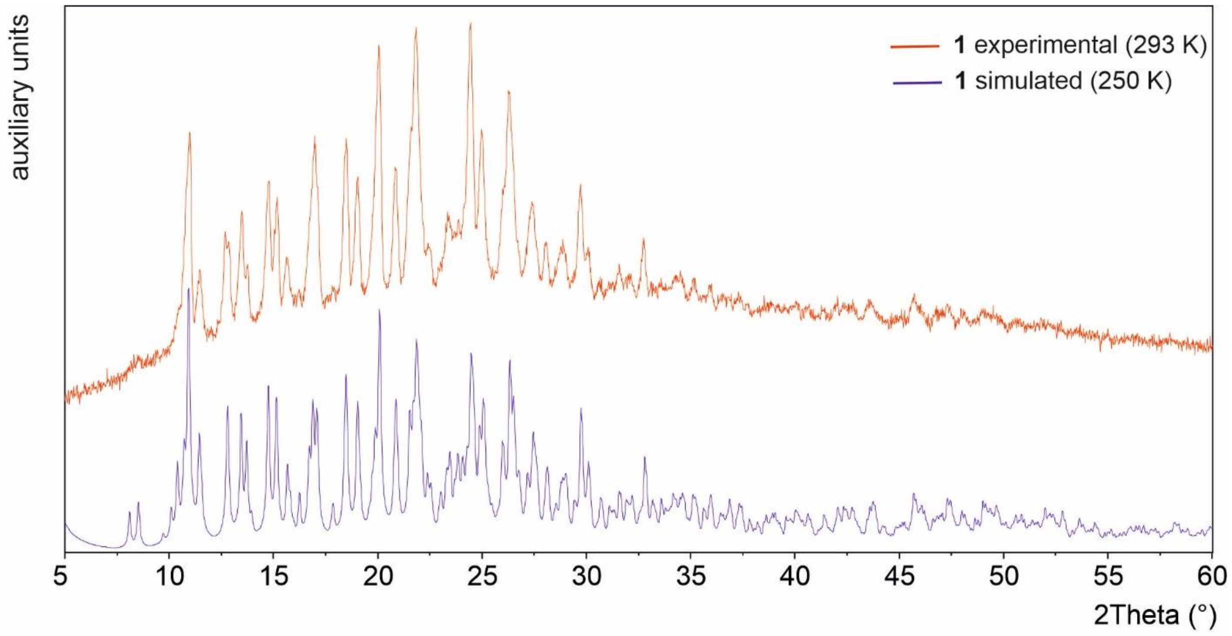

a)

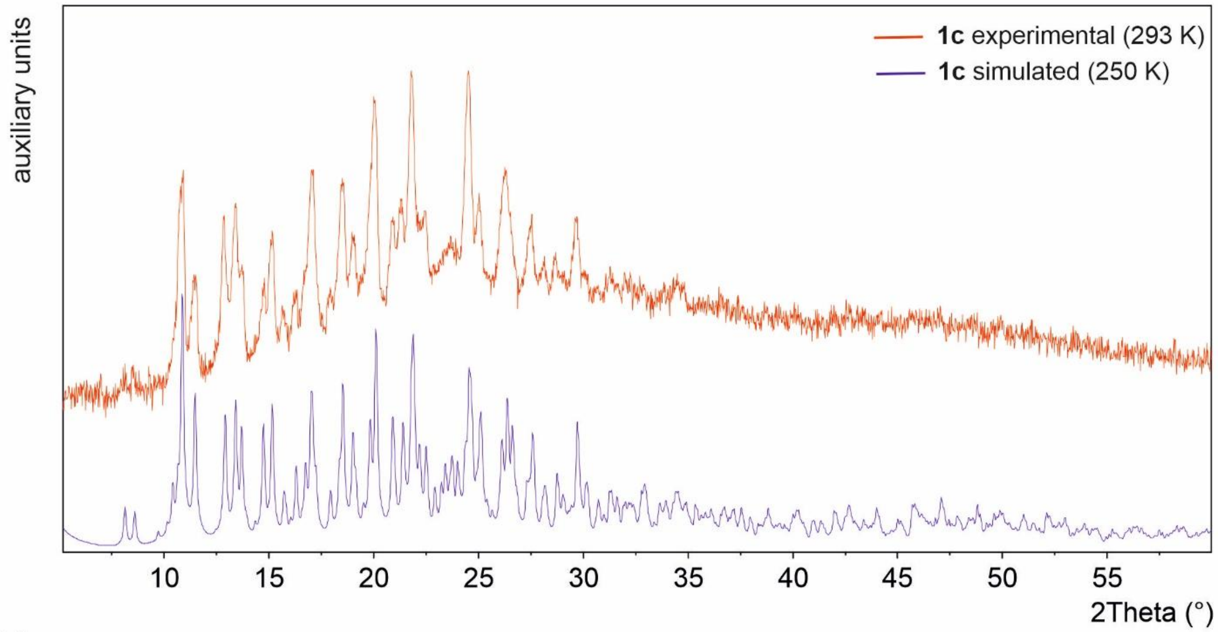

b)

Figure S15. PXRD diffractograms for **1** (a) and **1c** (b).

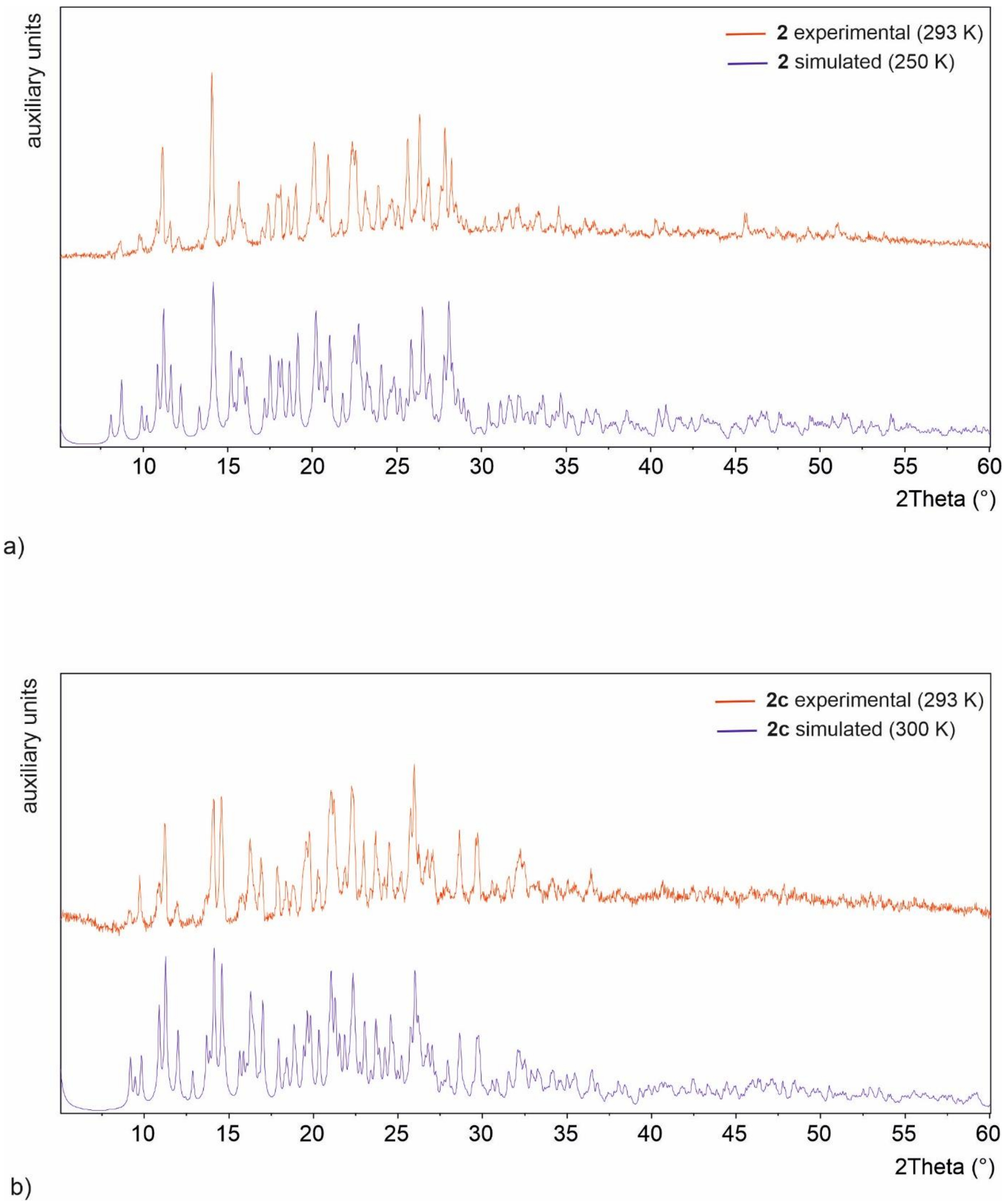

Figure S16. PXRD diffractograms for **2** (a) and **2c** (b).

Comment concerning intermolecular contacts in 1 and 1c

In the formation of the network of intermolecular contacts in **1**, the most important role is played by uncoordinated perchlorate anions. The perchlorate anion is disordered (17% of anions occupies an alternative position) at 250 K. It forms numerous intermolecular contacts of the type C-H···O(ClO_4^-), in which 1,2,3-triazole rings, methylene groups and phenyl rings of coumarin are involved. The acetonitrile molecule is also involved in the formation of contacts with an oxygen atom of a carbonyl group. There are two intramolecular C-H···N contacts involving 1,2,3-triazole rings.

Spin crossover does not involve serious changes of a network of intermolecular contacts. In the LS form a number of intermolecular contacts remains practically unchanged. It is worth noting that the intramolecular C-H···N contacts involving the triazole rings are still present but they are shorter comparing to a HS state. In most cases the C-H···O distances shorten slightly, which is a rather an expected effect of a crystal lattice compression.

In **1** only a part of the ligand molecules participates in a photocyclization process. The lack of long-range ordering of dimeric molecules and ligand molecules not taking part in the photoconversion means that we are dealing with an average structure in the form of a ligand molecules disorder. Although the analysis of intermolecular contacts in **1c** indicates that a very dense network is formed (in which perchlorate anions again play the main role), it is not possible to make a reasonable analysis of intermolecular contacts, especially for coumarin fragments taking part in photoconversion. The most striking difference is an increased (up to four) number of the intramolecular C-H···N contacts involving the triazole rings.

Comment concerning intermolecular contacts in 2 and 2c

Overall, the number of intermolecular contacts in a HS form of **2** (250 K) is very close to that found for **1**. It should be noted that in compound **2** there are no uncoordinated acetonitrile molecules in the crystal lattice. Similarly to the compound **1** a high spin form of complex **2** is characterized by a formation of a dense network of intermolecular contacts between perchlorate anions and triazole rings, methylene groups, and phenyl rings. Similarly to **1** two intramolecular contacts C-H···N established between triazole rings are present. In a relation to the compound **1** a new type of intramolecular C-H···N contact appears, which involves phenyl and triazole rings. In addition, a new type of interaction C-H···O(C=O) between lactone rings occurs, in which the carbonyl group participates. In general, HS → LS transition does not involve serious changes in the intermolecular interaction network. The donor-acceptor distances change by less than 0.1 Å.

In a contrast to the SCO process in **2**, the **2** → **2c** a photoconversion process involves an increase in a number of intermolecular contacts and entails much more substantial changes in the intermolecular interaction network. The most important difference not observed before depends on the formation of an additional weak contact between the triazole rings. As a consequence, all six triazole rings are additionally bonded by a network of intramolecular contacts. Moreover, carbonyl group no longer interacts with the phenyl ring of the ligand molecule. As anticipated, perchlorate anions participate in the formation of a dense network of intermolecular contacts similarly to abovementioned examples.
In comparison to intermolecular contacts changes related to spin crossover in **1** and **2**, HS → LS transition in **2c** are associated with a significant increase of a number of the intermolecular contacts.

DFT modelling.

IR spectra. DFT calculations of the vibrations observed in the IR spectra on light irradiation were performed. The comparison of the observed changes in the 1100-1800 cm^{-1} region reveal no particular changes between the solvated **1** and nonsolvated **2**. On the other hand it is reasonable to assume that the spectra of in this area are not sensitive to the spin state. Thus, considering the economy of the computation, for the modelling we choosed the monomeric complex based on the X-ray strucuture of the low-spin **2** and the model of low-spin **2c** based on its X-structure.

The model of the latter is shown in the Figure S17 below, the corresponding pdb structures are attached as Supplementary Information.

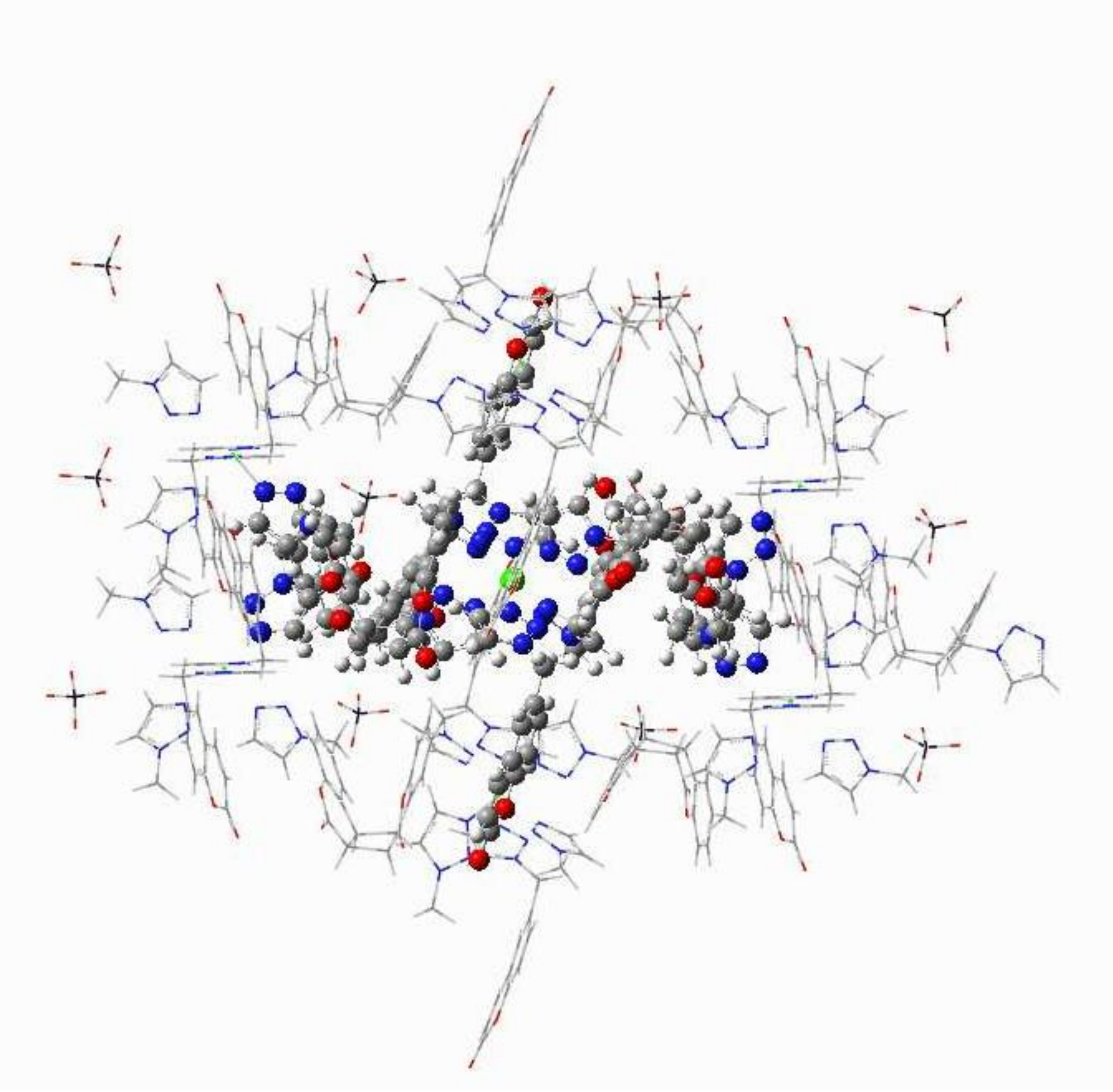

Figure S17. The structural model used for the DFT modelling of **2c**. The figure plane corresponds to *bc* crystallographic plane. The model involves 7 Fe(II) centres, the one in the middle (shown as balls and stick model) reveals the exact environment with four dimerised ligands bridging the central Fe atom and the four neighbours. The eight remaining neighbors (shown for clarity as wireframe model) have (with one exception) they ligands bridging to the outer part of the bc plane replaced with methyl triazol. With 12 perchlorate anions (not optimised) the whole system has a charge of +2. For the model of **2c** a method based on the frozen-matrix approach[8] was applied, involving the geometry optimisation of the central unit only (see Fig. S17).

The used model of the monomeric **2** is shown in Figure S18.

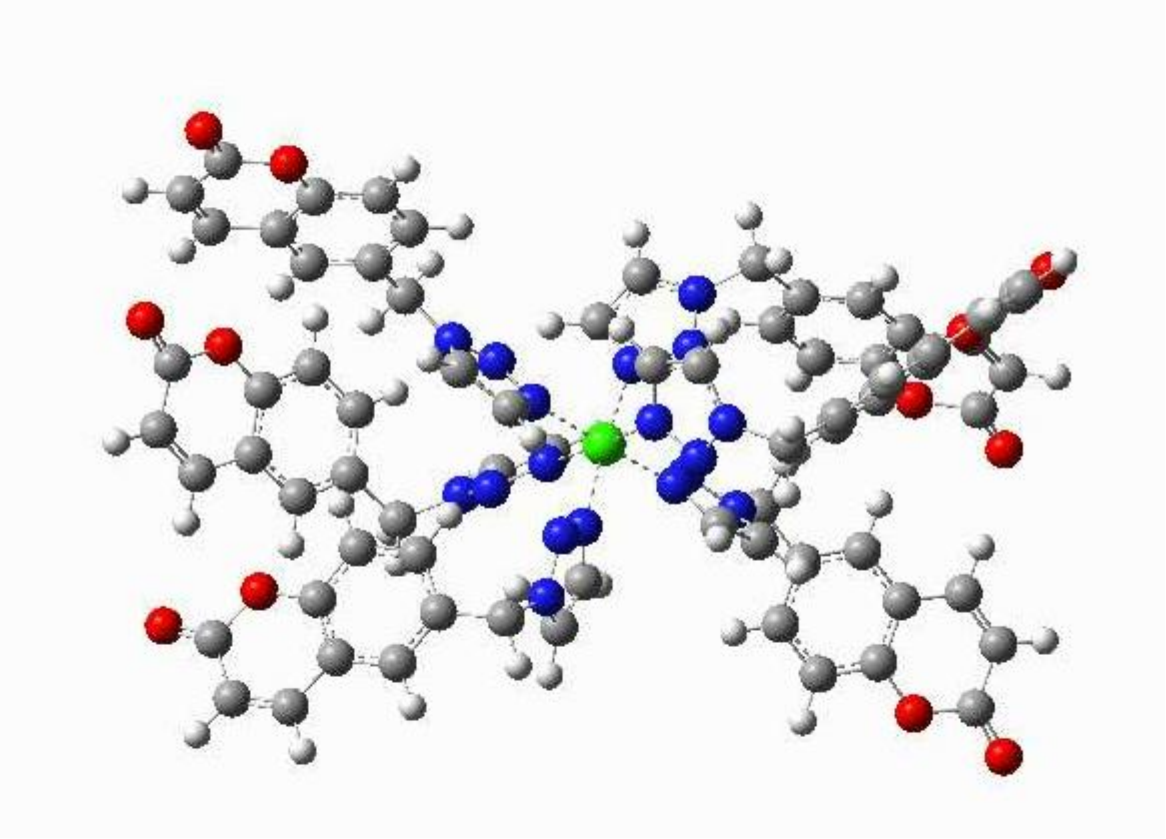

Figure S18 The structural model used for the DFT modelling of **2.** The dicationic species was optimised.

For both cases the CAM-B3LYP functional[9] with CEP-31g basis[10] set were applied with Grimme's D3 dispersion correction.[11]

Reliability of the DFT assignment of the strain energy differences.

As stated in the main text the energy decomposition of the strain energy difference between the dimerised ligand in the HS and LS **2c** complex has been performed using the DFT calculated electronic energies for the geometries obtain with X-ray diffraction. The TPSS functional with tzvp basis set and Grimmes D3 dispersion corrections were used. In order to test how robust the obtained strain energy differences are depending on the used DFT tools we performed the additional computations using the **meta-generalized gradient approximation functionals** TPSS and M06[12], and the hybrid B3LYP[13], and CAM-B3LYP[9] functionals with use of tzvp, qzvp[14], LANL2DZ[15] and 6-311++G[16] basis sets, applying the D3 dispersion correction.

The results are shown in the subsequent Tables S5a-S5f.

Table S5a. Electronic energy differences ΔE (kJ·mol^{-1}) of photodimerised ligands corresponding to the whole molecules in the HS and LS states of **2c**. Energy differences were taken between the HS and LS configurations (E_{HS}-E_{LS}). Thus, positive values reflect a higher strain for the related HS structures. The overall mean value is given in bold, the mean value for a given basis is given in underlined, the mean values for a given functional are given in italics. Standard deviations are given.

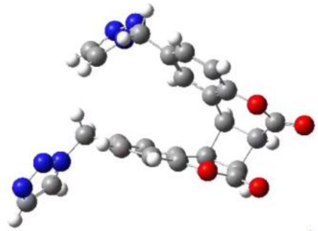

	TZVP	QZVP	LAN-L2DZ	6-311++G	Mean value
TPSS	234	227	268	244	*243(16)*
B3LYP	222	214	258	230	*231(17)*
CAM-B3LYP	215	209	251	225	*225(16)*
M06	218	210	251	230	*227(15)*
Mean value	222(7)	215(7)	257(7)	232(7)	**232(12)**

Table S5b. Electronic energy differences ΔE (kJ·mol^{-1}) of photodimerised ligands corresponding to the cyclobutane together with coumarin fragments in the HS and LS states of **2c**. Energy differences were taken between the HS and LS configurations (E_{HS}-E_{LS}). Thus, positive values reflect a higher strain for the related HS structures. The overall mean value is given in bold, the mean value for a given basis is given in underlined, the mean values for a given functional are given in italics. Standard deviations are given.

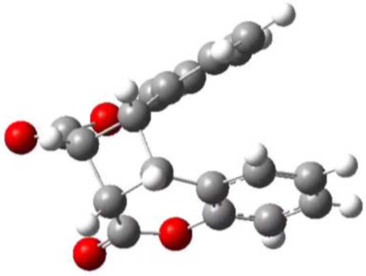

	TZVP	QZVP	LAN-L2DZ	6-311++G	Mean value
TPSS	131.5	128	149	136	*136(8)*
B3LYP	125	121	144	129	*130(9)*
CAM-B3LYP	133	117	140	125	*129(9)*
M06	123	118	140	128	*127(8)*
Mean value	128(4)	121(4)	143(4)	129.5(4)	**130(6)**

Table S5c. Electronic energy differences ΔE (kJ·mol^{-1}) of photodimerised ligands corresponding to the phenyl fragments in the HS and LS states of **2c**. Energy differences were taken between the HS and LS configurations (E_{HS}-E_{LS}). Thus, positive values reflect a higher strain for the related HS structures. The overall mean value is given in bold, the mean value for a given basis is given in underlined, the mean values for a given functional are given in italics. Standard deviations are given.

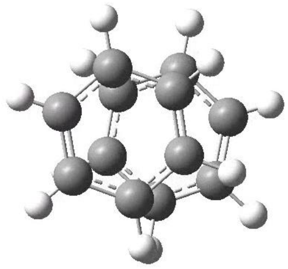

	TZVP	QZVP	LAN-L2DZ	6-311++G	Mean value
TPSS	96	93	106	97	*98(5)*
B3LYP	92	89	104	93	*94.5 (6)*
CAM-B3LYP	90	87	101	91	*92(5)*
M06	90	87	100	92	*92(4)*
Mean value	92(2)	89(2)	103(2)	93(2)	**94(4)**

Table S5d. Electronic energy differences ΔE (kJ·mol^{-1}) of photodimerised ligands corresponding to the cyclobutane together with lactone fragments in the HS and LS states of **2c**. Energy differences were taken between the HS and LS configurations (E_{HS}-E_{LS}). Thus, positive values reflect a higher strain for the related HS structures. The overall mean value is given in bold, the mean value for a given basis is given in underlined, the mean values for a given functional are given in italics. Standard deviations are given.

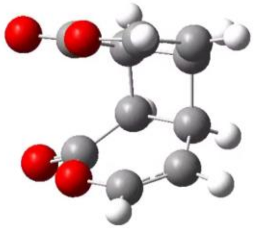

	TZVP	QZVP	LAN-L2DZ	6-311++G	Mean value
TPSS	**32**	30	41	35	*34.5(4)*
B3LYP	28	26	38	32	*31(5)*
CAM-B3LYP	26	25	36	30	*29(4)*
M06	27	25	36	31	*30(4)*
Mean value	28(2)	26,5(2)	38(2)	32(2)	**31(4)**

Table S5e. Electronic energy differences ΔE (kJ·mol^{-1}) of photodimerised ligands corresponding to the triazole fragments in the HS and LS states of **2c**. Energy differences were taken between the HS and LS configurations (E_{HS}-E_{LS}). Thus, positive values reflect a higher strain for the related HS structures. The overall mean value is given in bold, the mean value for a given basis is given in underlined, the mean values for a given functional are given in italics. Standard deviations are given.

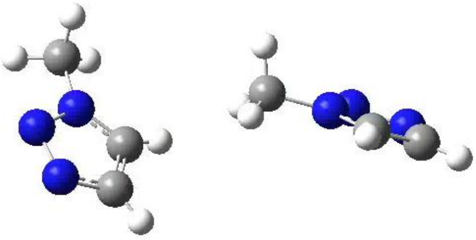					
	TZVP	QZVP	LAN-L2DZ	6-311++G	Mean value
TPSS	**62**	60	76	68	*66.5(6)*
B3LYP	57	55	72	64	*62(6)*
CAM-B3LYP	54	52	69	60	*59(7)*
M06	55	53	69	62	*60(6)*
Mean value	<u>57(3)</u>	<u>55(3)</u>	<u>71.5(3)</u>	<u>63.5(3)</u>	62(5)

Table S5f. Electronic energy differences ΔE (kJ·mol^{-1}) of photodimerised ligands corresponding to the isolated cyclobutane fragments in the HS and LS states of **2c**. Energy differences were taken between the HS and LS configurations (E_{HS}-E_{LS}). Thus, positive values reflect a higher strain for the related HS structures. The overall mean value is given in bold, the mean value for a given basis is given in underlined, the mean values for a given functional are given in italics. Standard deviations are given.

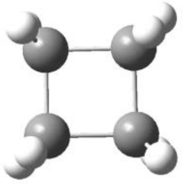					
	TZVP	QZVP	LAN-L2DZ	6-311++G	Mean value
TPSS	**36**	34	38	35	*136(1)*
B3LYP	34	33	37	34	*34.5(1)*
CAM-B3LYP	34	33	37	34	*34.5(1)*
M06	34	33	36	30	*33(2)*
Mean value	<u>34.5(1)</u>	<u>33(0.5)</u>	<u>37(1)</u>	<u>33(2)</u>	34.5(1)

References

---

[1] G. M. Sheldrick, *Acta Crystallogr., Sect. A: Found. Adv*., **2015**, 71 , 3.

[2] G. M. Sheldrick, *Acta Crystallogr., Sect. C: Struct. Chem*., **2015**, 71, 3.

[3] O. V. Dolomanov, L. J. Bourhis, R. J. Gildea, J. A. K. Howard, H. Puschmann, *J. Appl. Cryst.,* **2009**, 42, 339.

[4] Gaussian 16, Revision A.03, M. J. Frisch, G. W. Trucks, H. B. Schlegel, G. E. Scuseria, M. A. Robb, J. R. Cheeseman, G. Scalmani, V. Barone, G. A. Petersson, H. Nakatsuji, X. Li, M. Caricato, A. V. Marenich, J. Bloino, B. G. Janesko, R. Gomperts, B. Mennucci, H. P. Hratchian, J. V. Ortiz, A. F. Izmaylov, J. L. Sonnenberg, D. Williams-Young, F. Ding, F. Lipparini, F. Egidi, J. Goings, B. Peng, A. Petrone, T. Henderson, D. Ranasinghe, V. G. Zakrzewski, J. Gao, N. Rega, G. Zheng, W. Liang, M. Hada, M. Ehara, K. Toyota, R. Fukuda, J. Hasegawa, M. Ishida, T. Nakajima, Y. Honda, O. Kitao, H. Nakai, T. Vreven, K. Throssell, J. A. Montgomery, Jr., J. E. Peralta, F. Ogliaro, M. J. Bearpark, J. J. Heyd, E. N. Brothers, K. N. Kudin, V. N. Staroverov, T. A. Keith, R. Kobayashi, J. Normand, K. Raghavachari, A. P. Rendell, J. C. Burant, S. S. Iyengar, J. Tomasi, M. Cossi, J. M. Millam, M. Klene, C. Adamo, R. Cammi, J. W. Ochterski, R. L. Martin, K. Morokuma, O. Farkas, J. B. Foresman, and D. J. Fox, Gaussian, Inc., Wallingford CT, **2016**.

[5] L. de Benneville, R. Connor, *J. Am. Chem. Soc.,* **1940**, 62, 11, 3067.

[6] F. Leonetti, A. Favia, A. Rao, R. Aliano, A. Paluszcak, R. W. Hartmann, A. Carotti, *J. Med. Chem.,* **2004**, 47, 6792.

[7] M. Kaźmierczak, M. Weselski, M. Siczek, J. A. Wolny, V. Schünemann, R. Bronisz, *Chem. Sci.*, **2025**, 16, 7884.

[8] J.A. Wolny, K. Gröpl. J. Kiehl, E. Rentschler, V. Schünemann, *Dalton. Trans.* **2024**, 53, 8391.

[9] T. Yanai, D. Tew, and N. Handy, *Chem. Phys. Lett.*, **2004**, 393, 51.

[10] a) W.J. Stevens, H. Basch, M. Krauss, *J. Phys. Chem.* **1984**, 81, 6026; b) W.J. Stevens, M. Krauss, H. Basch H, P.G. Jasien, *Can. J. Chem.* **1992**, 70, 612; c) T.R. Cundari, W.J. Stevens, *J. Chem. Phys.* **1993**, 98, 5555.

[11] S. Grimme , J. Antony, S. Ehrlich, H. Krieg H *J. Chem. Phys.* **2010**, 132, 154104.

[12] Y. Zhao, D. G. Truhlar, *J. Chem. Phys.*, **2006**, 125, 194101, 1.

[13] A. D. Becke, *J. Chem. Phys.*, **1993**, 98, 5648.

[14] F. Weigend, R. Ahlrichs, *Phys. Chem. Chem. Phys.*, **2005**, 7, 3297.

[15] P. J. Hay, W. R. Wadt, *J. Chem. Phys.*, **1985**, 82, 299.

[16] R. Krishnan, J. S. Binkley, R. Seeger, J. A. Pople, *J. Chem. Phys.* **1980**, 72, 650.